Volume 29
DOE/DP40200-38

LLE Review

Quarterly Report

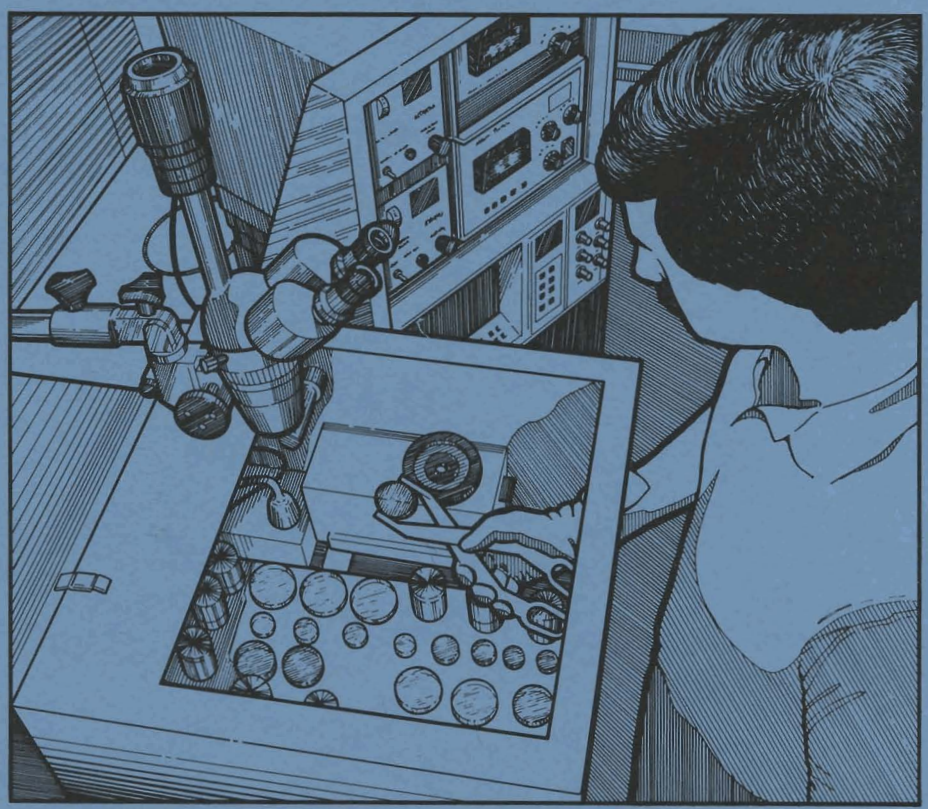

October–December 1986

Laboratory for Laser Energetics
College of Engineering and Applied Science
University of Rochester
250 East River Road
Rochester, New York 14623-1299

Volume 29
DOE/DP40200-38

LLE Review

Quarterly Report

Editor: J. Delettrez
(716) 275-5374

October–December 1986

Laboratory for Laser Energetics
College of Engineering and Applied Science
University of Rochester
250 East River Road
Rochester, New York 14623-1299

IN BRIEF

This volume of the LLE Review, covering the period October–December 1986, contains an analysis of the effect of laser illumination nonuniformity on the analysis of transport experiments; a review of measurements carried out with a high-resolution XUV spectrometer; a study of shock launching in silicon crystals; measurements of thermal conductivity in dielectric thin films; and the National Laser Users Facility activities for this period. Finally, the laser activities on GDL and OMEGA are summarized.

The following are highlights of the research reports contained in this issue:

- A method has been developed to study from simulations the effect of laser illumination nonuniformity on the interpretation of the transport experiments carried out with the 24 UV beams of OMEGA. The results indicate that laser illumination nonuniformity can lead to deduction of erroneously high values of the heat flux. Estimates of the levels of laser illumination nonuniformities are discussed.
- A high-resolution extreme UV spectrograph was used to study relativistic and quantum electrodynamic effects in high atomic number elements, to measure conditions in the coronal plasma, and to diagnose transitions in x-ray laser research.
- The temporal variation of lattice spacing due to shocks launched into laser-irradiated silicon crystals was studied by Bragg x-ray diffrac-

tometry with pulsed x rays. Lattice compression and the onset of rarefaction as the pressure pulse decayed were measured.

- A method has been developed for measuring the thermal conductivity of dielectric materials in thin-film form. We have found that thin films of SiO_2 and Al_2O_3, deposited on silicon substrates, exhibit thermal conductivities several orders of magnitude below those of their solid counterparts. MgF_2 films, however, seem to behave more like bulk single-crystal MgF_2.
- A 25th beam from the output of the GDL active mirror laser system has been transported through the laboratory to the OMEGA target bay and focused onto a target in the OMEGA chamber.

CONTENTS

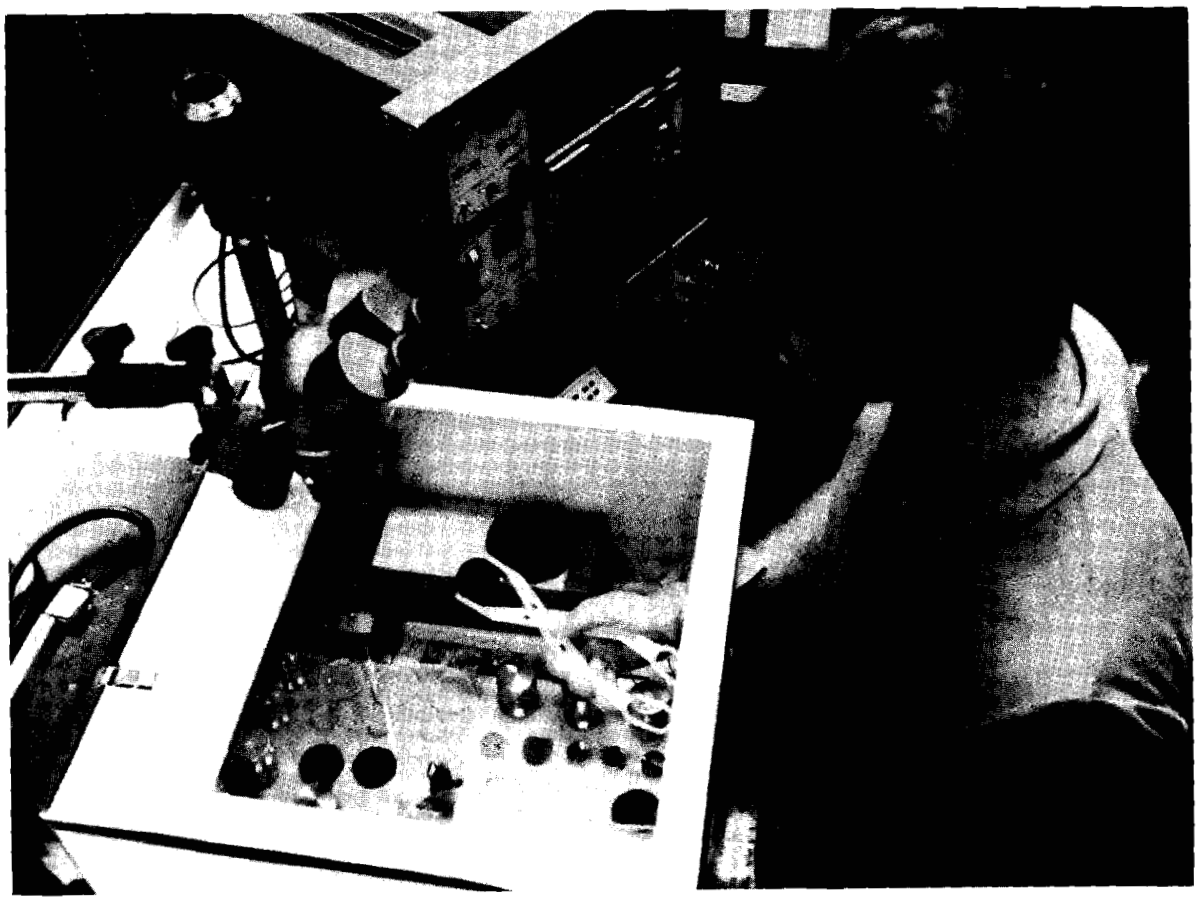

Undergraduate optics student Scott Gilman is loading samples into a high-precision thermal comparator apparatus. This instrument is used to measure the thermal conductivity in dielectric thin films.

Section 1
PROGRESS IN LASER FUSION

1.A Effect of Laser Illumination Nonuniformity on the Analysis of Time-Resolved X-Ray Measurements in UV Spherical Transport Experiments

Introduction

Thermal transport plays a key role in direct-drive laser fusion[1] because it affects the efficiency of the ablation process that drives the implosion of laser-driven targets. In transport experiments, the thermal electron flux is not measured directly but is inferred from measurable quantities. One such quantity is the burn-through rate of the heat front through a material that contains one or more x-ray-emitting signature layers.[2–6] Simulations are then carried out with a hydrodynamic code in which the thermal electron flux is characterized by the value of the flux limiter f required to replicate the experimental observations;[7] the flux limiter is the adjustable parameter in the definition of the free-streaming limit of the heat flux,

$$Q_f = f n_e (kT_e)^{3/2}/m_e,$$

which is the upper-limit on the heat flux. Experiments in spherical geometry have inferred various levels of flux inhibition, from as low as $f = 0.06$ with 1050-nm laser radiation,[3] to values of $f > 0.1$ at various laser wavelengths.[2,4,6] In all these experiments, the analysis of the measurements assumed that the laser intensity distribution on the target surface did not differ appreciably from the average intensity.

In a series of transport experiments conducted at LLE,[8] experimental results were such that the assumption of uniform laser intensity distribution could not hold any more. In these experiments, the

temporal dependence of the mass-ablation rate of spherical targets irradiated with UV-laser light was measured using time-resolved x-ray spectroscopy. The measured mass-ablation rate was found to be larger by a factor of 2 than that obtained in simulations with uninhibited heat flow, yet the scalings of the mass-ablation rate with absorbed intensity were in agreement. One of the reasons advanced for the discrepancy between experiment and simulation was that using only six beams of the OMEGA laser system at 351 nm produced a nonuniform illumination pattern on the targets.

The effect of laser illumination nonuniformity on the interpretation of thermal transport experiments has not been previously studied in detail. Yet, neglecting nonuniformity can lead to erroneous conclusions when the analyis of the thermal transport is based on spectroscopic diagnostics, which usually do not incorporate high spatial resolution. Nonuniformities in the multibeam illumination of spherical targets arise from two sources: nonuniformities in the individual beams and the result of the overlap of the individual beam distributions on the target surface.[9] The beam geometry and beam overlap lead to long-wavelength variations that have little effect on transport experiments. The nonuniformities that do affect the interpretation of transport experiments occur in the individual beams of the frequency-tripled OMEGA glass laser system and manifest themselves as small regions (< 20 μm in diameter in the target plane) of very high intensity, or "hot spots." If the hot spots contain a sufficiently large fraction of the total energy, their presence in the intensity distribution on the surface of the target can lead to the conclusion that the heat flux inferred from spectroscopic diagnostics is larger than would be obtained for a given nominal intensity. Such hot spots produce stronger line emission in the case of time-integrated burn-through experiments, or earlier emission in the case of time-resolved burn-through experiments, than expected from nominal intensity. This effect is more important for laser illumination at 351 nm than at 1060 nm because lateral thermal smoothing is not as effective at the shorter wavelength.[10] Illumination nonuniformity could also explain some of the discrepancies between results from various laboratories, since each laser system has its own distinctive illumination pattern resulting from differences in optics and beam quality.

In this report we present an analysis of recent time-resolved burn-through measurements on spherical targets and discuss the effect of illumination nonuniformities on the interpretation of the results. The analysis shows that taking into account the estimated level of nonuniformity of the laser illumination can advance the onset of the x-ray signature lines by about 100 ps and also affect the temporal shape of the line emission. Intensities larger than three times the nominal intensities were required to obtain agreement between the measured and computed onset times of signature lines. Also, the mass-ablation rate was measured for times past the peak of the pulse, when the rate had been predicted to drop rapidly.[8]

The measurements discussed in this report were part of a series of transport experiments carried out at 351 nm on the 24-beam OMEGA

laser system at LLE.[11] This system produces energies up to 2 kJ in approximately Gaussian-shaped pulses of about 600-ps (FWHM) duration. The laser beams are focused on the target in such a way as to provide the most uniform irradiation conditions.[12] The targets were solid glass spheres of two nominal diameters (300 μm and 600 μm), coated with 2 μm to 16 μm of parylene (CH) and suspended on submicron-diameter glass stalks. The nominal (average) intensities on target ranged from 3×10^{14} to 1×10^{15} W/cm^2.

The diagnostics included plasma calorimeters and charge collectors to characterize the absorption and the plasma blowoff, x-ray photography of the target, and time-resolved and time-integrated x-ray spectroscopy. In this report, emphasis is placed on time-resolved spectroscopic results obtained from the SPEAXS instrument,[13] in which an elliptically curved mica crystal analyzer was used to disperse the x-ray spectrum (1.5-keV to 3.2-keV range) onto the slit of an x-ray streak camera. The temporal characteristics of the burn-through were obtained by measuring the time of onset of the silicon Hβ line emission for targets with varying thicknesses of CH. A timing fiducial signal was generated by quadrupling the frequency of part of the main laser pulse obtained from mirror leakage and focusing it to a section of the photocathode consisting of a 200-Å layer of aluminum on mica.[14] The time of onset was defined as the time at which the intensity of a certain line emission exceeded the CH continuum emission by a factor of 2.

Details of the Analysis

The time-resolved spectra for two series of shots were digitized: one series at 3×10^{14} W/cm^2 with CH thicknesses of 0, 2, 4, and 6 μm, and the other at 1×10^{15} W/cm^2 with CH thicknesses of 0, 4, 8, and 12 μm. Superpositions of the digitized traces for the Si Hβ lines at each laser intensity are shown in Fig. 29.1. Time is measured relative to the peak of the laser pulse, as determined from the fiducial, and the vertical axis is the intensity of the line emission obtained from the measured *D*-log exposure curves for the streak camera recording film. The continuum emission was subtracted in order to obtain a clearly defined onset time. In marginal burn-through cases, such as for the 12-μm CH case in Fig. 29.1(b), the location of the onset of the line emission is difficult to determine from the lineout, but it can be clearly seen in the original photograph.

Simulations were performed with the one-dimensional Lagrangian hydrodynamic code *LILAC*,[15] which includes ray tracing, Thomas-Fermi equation of state, and multigroup diffusion radiation transport. The ray tracing is carried out using the azimuthally averaged spatial profile of a typical beam; the inverse-bremsstrahlung opacity is corrected for the Langdon effect.[16] The electron thermal energy was transported using a flux-limited diffusion model in which the effective flux was defined as the minimum of the diffusion flux and the free-streaming flux (the sharp-cutoff method). The opacities used in the radiation transport calculation were obtained from the Los Alamos LTE astrophysical library.[17] A finely resolved x-ray energy grouping was used in these simulations to provide a better treatment of the x-ray

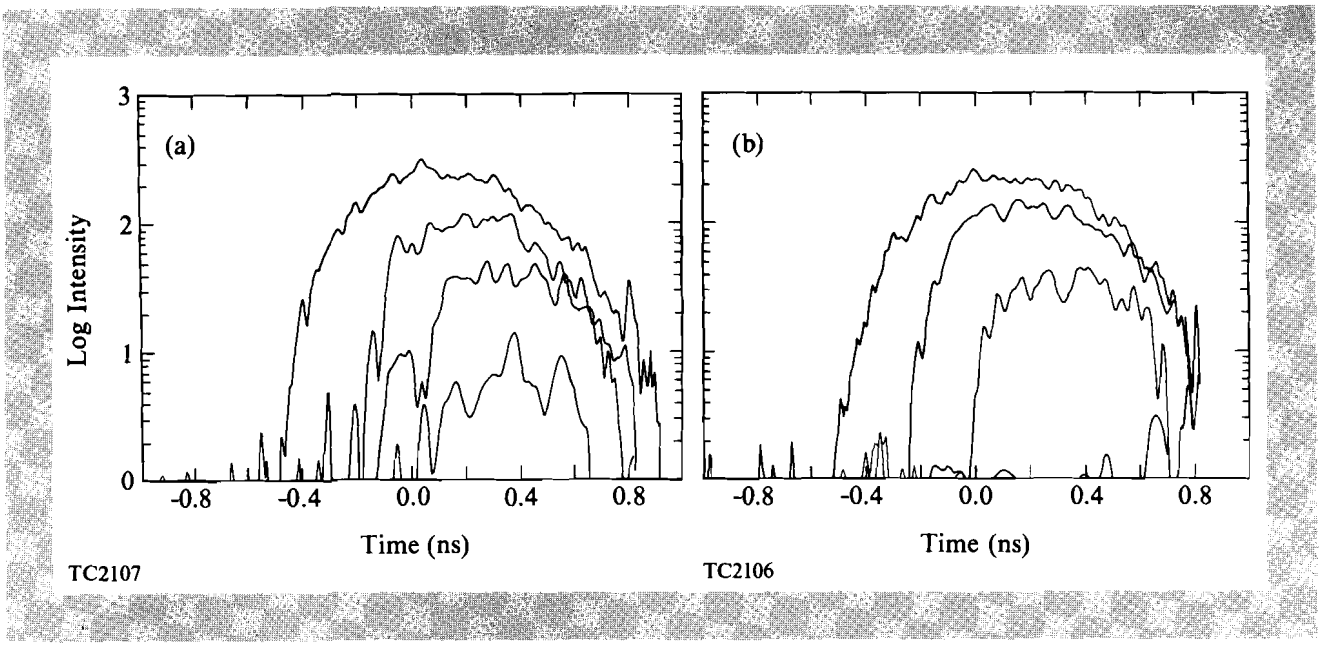

Fig. 29.1
Temporal emission of the Si Hβ line from SPEAXS:
(a) for 0, 2, 4, and 6 μm of CH over glass at 3×10^{14} W/cm^2;
(b) for 0, 4, 8, and 12 μm of CH at 1×10^{15} W/cm^2; the continuum has been subtracted.

line transport in the multigroup environment. The LTE line emissions presented in this report were obtained from the energy emitted from the narrow group (ΔE = 20 eV) that contained the Si Hβ line. Non-LTE considerations do not significantly affect the progress of the heat front through the low-Z plastic layer,[18] but may influence the onset of the silicon line emission. To appreciate this effect, the temporal line emission was also calculated with a non-LTE post-processor, which operates from *LILAC* results.[19]

To take into account the effect of the nonuniformity of the illumination of the target by a multibeam laser system, the overall laser intensity distribution on the target surface must be known. While it is not now possible to measure directly the intensity distribution at the target surface, one method of estimating this distribution is through the superposition of the equivalent-target-plane (ETP) intensity distributions of all the OMEGA laser beams. During this series of experiments, the illumination uniformity on target was estimated by using the measured two-dimensional ETP distribution from a single OMEGA beam as the input to a beam superposition code.[9] This code integrates the beam intensity distributions from all 24 beams of OMEGA, taking into account their position and orientation and the effects of refraction.[20] To approximate the differences between individual beam distributions, the two-dimensional ETP distribution was randomly oriented for different beams. The illumination uniformity is then characterized by decomposing the resulting spherical distribution into a histogram, shown in Fig. 29.2, which gives the relative energy in each intensity group on the target surface. The inset is a shaded contour plot of the target plane intensity distribution that was used. The plot contains several intensity hot spots about 15 μm to 20 μm across. The histogram shows a large peak at 1.4 times the nominal intensity I_0 (I_0 is the nominal intensity defined as the peak laser power divided by the initial target area) and residual energy at 1.9 I_0.

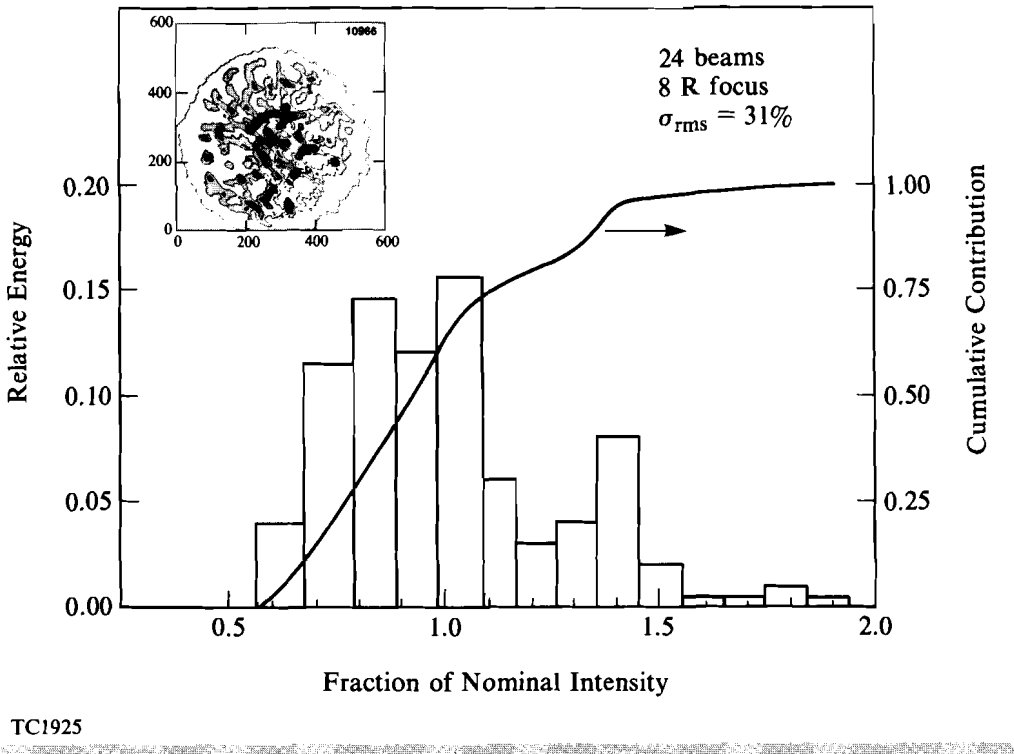

Fig. 29.2
Laser intensity variation on the target surface obtained from the equivalent-target-plane intensity distribution shown in the inset for 24 UV (351-nm) beams of OMEGA at 8-R (tangential) focus.

The distribution of intensities on target shown in Fig. 29.2 was used to estimate the temporal behavior of the x-ray line emission from the target in the presence of illumination nonuniformities. For a given target shot, *LILAC* simulations were performed for each of the 13 intensity distribution groups in Fig. 29.2. Each of these simulations produced a temporal emission of the silicon resonance lines (H- and He-like), which were then combined by weighting the emission for each intensity group by the fractional laser energy in that group.

Results of the Data Analysis

The first step in the simulations with *LILAC* was to adjust the flux limiter to agree at nominal intensity with the measured absorption fraction. This is in contrast with previous analyses of transport experiments[2–6] in which the goal had been to obtain agreement with the experimental transport data by varying the value of the flux limiter in the simulations; in most cases, agreement with the measured absorption fraction was not sought. This is not the goal in the present analysis. The absorption fraction was used to adjust the flux limiter because it is an integrated measurement that depends weakly on the intensity distribution. This weak dependence was verified by comparing the absorption fraction for a simulation at nominal intensity to the weighted-average absorption fraction: the relative difference in the absorption fraction was less than 10%. The flux limiter value of 0.06 (sharp cutoff) was used in all simulations unless otherwise noted.

The weighted-average temporal emissions for the Si Hβ line for the cases of Fig. 29.1 are shown in Fig. 29.3. The arrows denote the measured onset times obtained from the traces in Fig. 29.1. The weighted-average onset times are the same as those calculated for 1.4 I_0 because a significant amount of energy is present at that intensity (see Fig. 29.2). For all plastic thicknesses, the calculated onset times lag the measured times. In both series, the lag increases from about 100 ps for the smallest plastic thickness (excluding zero thickness) to 200 ps for the second thickness. For the largest thicknesses of plastic, which are marginal burn-through cases, the computed line emission is either nonexistent (12 μm in the high-intensity case) or much weaker than the measured line emission (6 μm in the low-intensity case). The effect of varying the flux limiter is illustrated in Fig. 29.4, where the temporal emission for a single thickness of plastic (4 μm at 3×10^{14} W/cm^2 and 8 μm at 1×10^{15} W/cm^2) is plotted at nominal laser intensity for increasing values of the flux limiter. The measured onset times are now denoted by shaded band with an estimated absolute error of ±50 ps. At 3×10^{14} W/cm^2, increasing the flux limiter to 0.08 decreases the onset time by only about 50 ps; further increasing the flux limiter has no effect. In this case, it is not possible to simulate correctly the measured onset time even with unrestricted Spitzer heat flow. At 1×10^{15} W/cm^2, the onset time is more sensitive to the flux limiter, but again, heat fluxes larger than classical Spitzer fluxes would be required to simulate the measured temporal line emission. Therefore, the experimental results can only be explained by the presence of significant energy in the laser intensity distribution at intensities larger than 1.5 I_0.

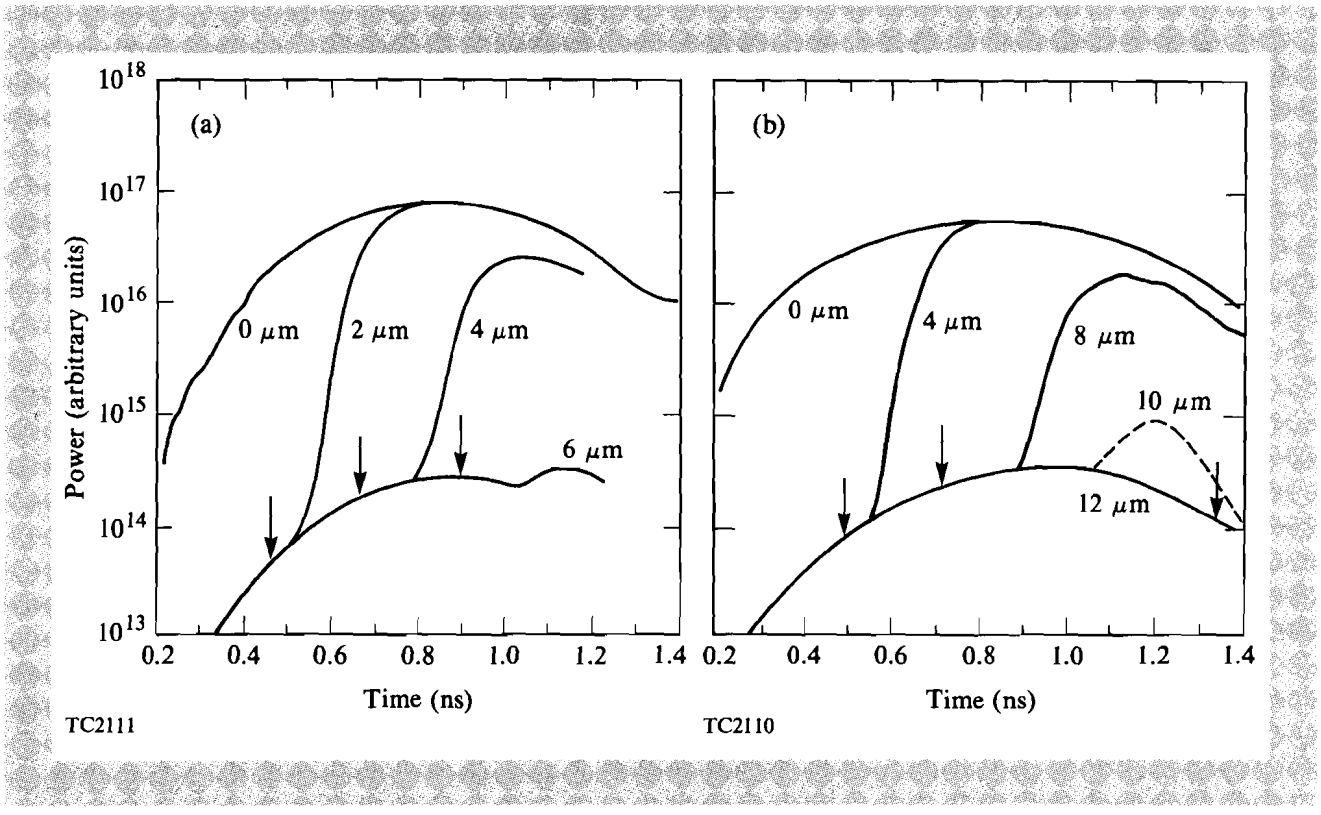

Fig. 29.3
Weighted-average temporal Si Hβ emission from *LILAC* calculated from the intensity distribution in Fig. 29.2:
(a) 3×10^{14} W/cm^2; and
(b) 1×10^{15} W/cm^2.
Arrows indicate the experimental times.

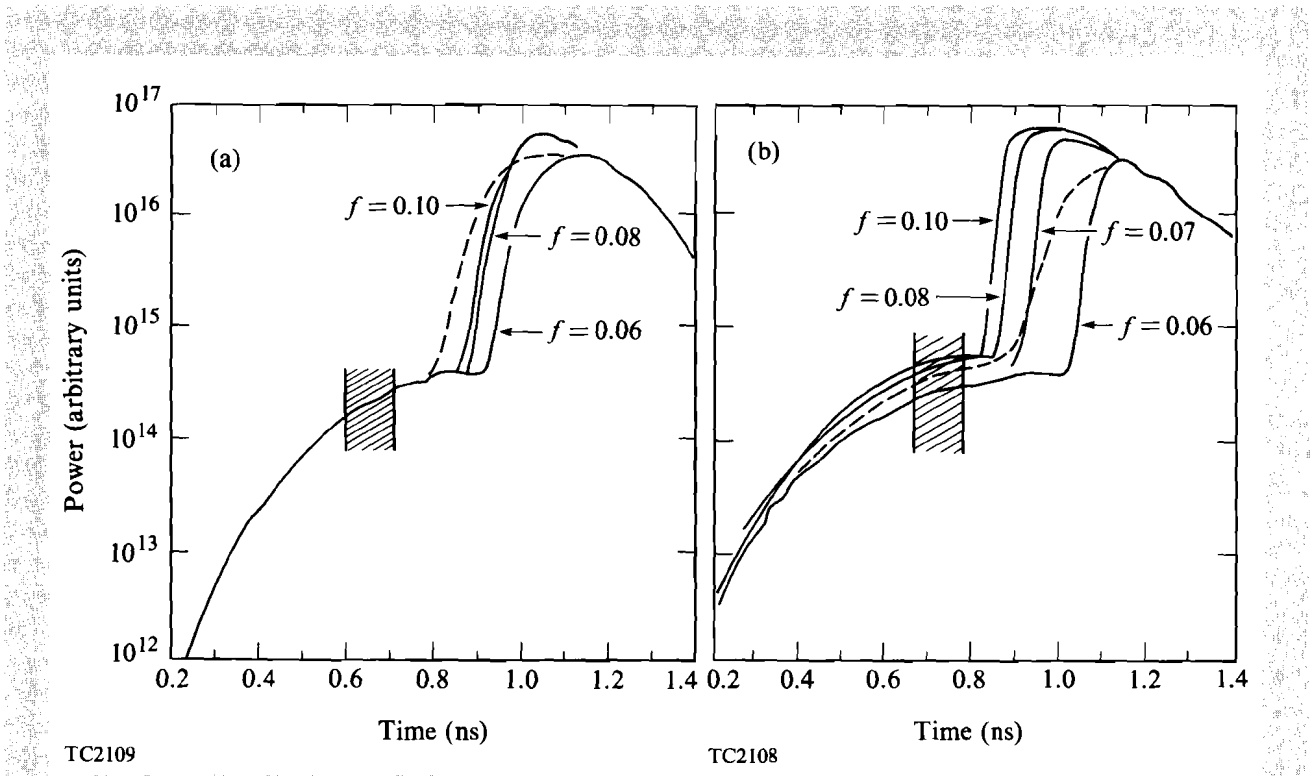

Fig. 29.4
Effect of varying the flux limiter on the onset of line emission and comparison between line emission at nominal intensity (solid lines) and the weighted-average line emission (dashed line):
(a) 3×10^{14} W/cm^2; and
(b) 1×10^{15} W/cm^2.

Based on the conclusion of Ref. 8—that absorbed intensities three times nominal would be required to match the measured mass-ablation rates with $f = 0.1$ (harmonic)—simulations were carried out for the two series of shots with incident intensities up to 3 I_0. The effect of varying the laser intensity from about 0.5 I_0 to 3 I_0 on the onset time of the Si Hβ line is shown in Fig. 29.5, where the onset time relative to the peak of the pulse is plotted as a function of the laser intensity on target normalized to the nominal intensity. The shaded bands represent the measured onset time with an estimated absolute error of ± 50 ps. In Figs. 29.5(a) and 29.5(b), for the case of the thinnest CH thickness, the heat front burns through to the glass for intensities below 0.6 I_0. For larger thicknesses of CH, line emission is produced only above a certain threshold intensity. Except for the two points nearest to the threshold intensity, the onset time scales as the laser intensity to some power that is different for each plastic thickness; the values of that power scaling range from 0.2 to 0.4. In Fig. 29.5, the onset times at 1.4 I_0 reflect the same lag with respect to the measured onset times, as seen in Fig. 29.3. For the series at 3×10^{14} W/cm^2, the calculated onset time at 3 I_0 agrees well with the experimental values for the three plastic thicknesses. This agreement, coupled with the fact that the onset times are not very sensitive to flux limiter values above 0.06, strongly suggests that some fraction of the incident laser energy must reside at intensities on target near 3 I_0 in the form of small, intense hot spots. At 1×10^{15} W/cm^2, agreement is obtained for 4 μm and 8 μm of plastic. For the 12-μm plastic case, the computed time is now about 200 ps ahead of the measured time. Attempts to increase that time further would result in the disappearance of the line emission, as

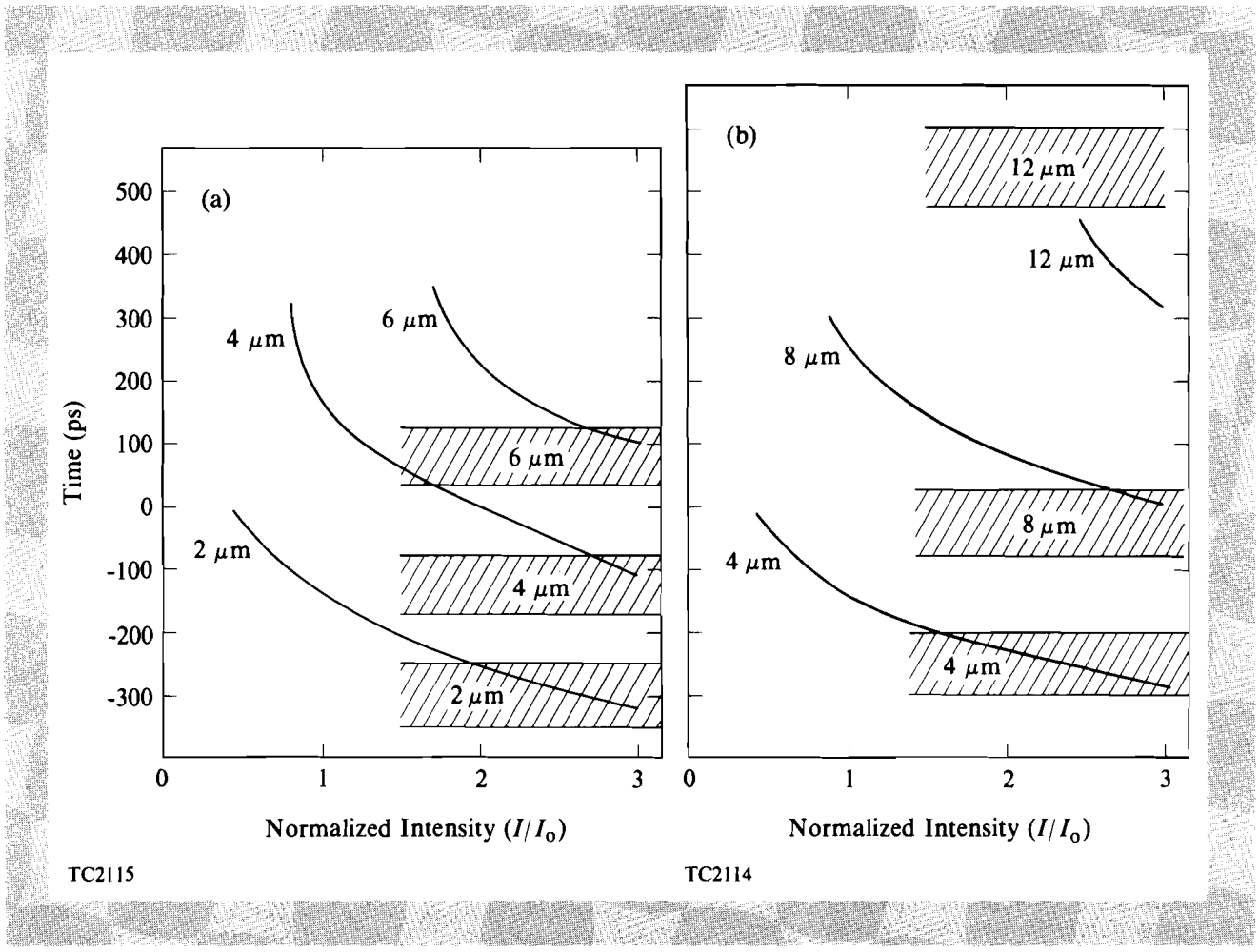

Fig. 29.5
Calculated onset times for the Si Hβ line as a function of the laser incident intensity; the shaded bands are the measured onset times and their uncertainty:
(a) 3×10^{14} W/cm^2; and
(b) 1×10^{15} W/cm^2.

can be seen in Fig. 29.5(b). The difficulty may lie in the fact that the onset time may not be known accurately because the burn-through is marginal at that plastic thickness. The argument that three times nominal intensity is required to explain the experimental results is not as straightforward at 1×10^{15} W/cm^2 as at 3×10^{14} W/cm^2, because the onset time is more sensitive to the flux limiter at the higher laser intensity; higher intensities and higher flux limiters are interchangeable in producing earlier onset times. Taken together, however, the analyses of the two series of shots strongly suggest that there is significant energy at 3 I_0 on the target surface.

It is difficult to estimate the fraction of the energy present in the laser intensity distribution above 1.5 I_0. One way is to consider the sensitivity of SPEAXS, which can be estimated experimentally from the amount of absorbed energy needed to observe the onset of the Si x-ray line emission: about 2% of the total absorbed energy (20 J to 30 J). But this is the amount of energy required to observe a signal above the noise level. The quantity of interest is the amount of energy that leads to an observable change in the onset time of the x-ray lines. This quantity could be estimated theoretically by modifying the laser intensity distribution of Fig. 29.2. The difficulty lies in how to distribute the additional energy above 1.5 I_0. Adding energy near

1.5 I_0 has less of an effect than adding the same amount of energy at 3 I_0. This is because, near 1.5 I_0, the increased emission is so close to the onset of the line emission from the known intensity distribution (Fig. 29.2) that it is added to the existing line emission rather than to the continuum emission, ahead of the onset, as is the case at 3 I_0. Because the actual laser intensity distribution between 1.5 I_0 and 3 I_0 is probably continuous, but not necessarily monotonically decreasing, it is not possible to get a precise estimate from theoretical considerations of the energy present in that intensity range. Reasonable estimates based on adding energy at 1.5 I_0 and 3 I_0 place this value at between 2% and 5% of the incident laser energy.

The method used in this report to estimate the effect of laser illumination nonuniformity on the interpretation of transport experiments has several limitations, one of which is that it does not include the effect of thermal smoothing. However, theoretical studies[10] indicate that lateral heat flow contributes little to thermal smoothing for nanosecond-duration 351-nm pulses on spherical targets. Another possible limitation arises from the fact that the illumination was estimated with the distribution of only a single beam of OMEGA rather than with those of all 24 beams. The quality of the frequency tripling cells varies from beam to beam. The single-beam-laser intensity distribution used in the calculation of the intensity distribution on the target surface was obtained for a beam produced by a crystal cell of average quality, not by the worst one. Finally, because the spatial resolution of the ETP distribution was limited to about 20 μm, the hot spots may be smaller than 20 μm and their intensity could possibly be larger than presently measured. Consideration of these limitations leads to the conclusion that the actual intensity distribution on target probably contains a larger fraction of the laser energy at the high intensities than in the estimated intensity distribution shown in Fig. 29.2.

Effect of Illumination Uniformity

Fig. 29.4 illustrates how including the illumination nonuniformity in the analysis of time-resolved spectroscopic measurements can affect conclusions regarding the thermal transport. This is seen by comparing onset times from nominal intensity simulations for varying values of the flux limiter with the weighted-average times. In Fig. 29.4(a), no values of the flux limiter will give the same onset time as the weighted-average onset time because the thermal transport is not sensitive to the flux limiter for $f > 0.08$. At 1×10^{15} W/cm^2, the weighted-average onset time is obtained for $f = 0.07$, not very different from the nominal value of $f = 0.06$. It should be noted that part of the change in the onset time is also due to the increase in the absorption fraction associated with the increase in the flux limiter. An immediate conclusion is that, in order to match computed onset times to measured onset times, simulations with nominal intensity would yield larger values of the flux limiter than would be obtained when illumination nonuniformities are included; in fact, at low intensity, the heat flux would have to be larger than classical heat flux to match the measured onset times. The inclusion of illumination nonuniformity in the simulations also results in the presence of line emission that would

not be produced at the nominal intensity: for example, at 3×10^{14} W/cm^2 and 6 μm of CH, line emission occurs only for laser intensities above 1.5 I_0. Another effect of including the illumination nonuniformity arises from the fact that the onset times are different for each of the illumination intensities on the target. While the rise time from the simulations at individual intensities is very steep, typically less than 50 ps (see Fig. 29.4), the weighted-average emission has a slower rise time—longer than 100 ps. This is because the various illumination intensities contribute to the emission rise at different times. Thus, x-ray emission rise times, which are large in the experiment (see Fig. 29.1), are sensitive to the illumination uniformity: more uniform illumination will lead to steeper rise time.

The onset of the calculated x-ray line emission and its rise times can also be affected by the inclusion of non-LTE atomic physics in the simulation. Because non-LTE ionization lags behind LTE ionization, one can expect the emission onset to occur later and the rise time to be longer for the non-LTE case. Simulations that included non-LTE post processing resulted in small differences in the line-emission onset time. In Fig. 29.6 are plotted the LTE and the non-LTE temporal line emission for a given plastic thickness at both laser intensities. At 3×10^{14} W/cm^2, the non-LTE onset time lags the LTE time by about 50 ps–70 ps; at 1×10^{15} W/cm^2, there is no lag. It is not obvious why there should be a difference between the two cases. The other differences observed were a longer rise time for the non-LTE

Fig. 29.6
Comparison between LTE (solid line) and non-LTE (dashed line) line emission for Si Hβ:
(a) 4 μm of CH at 3×10^{14} W/cm^2; and
(b) 8 μm of CH at 1×10^{15} W/cm^2.

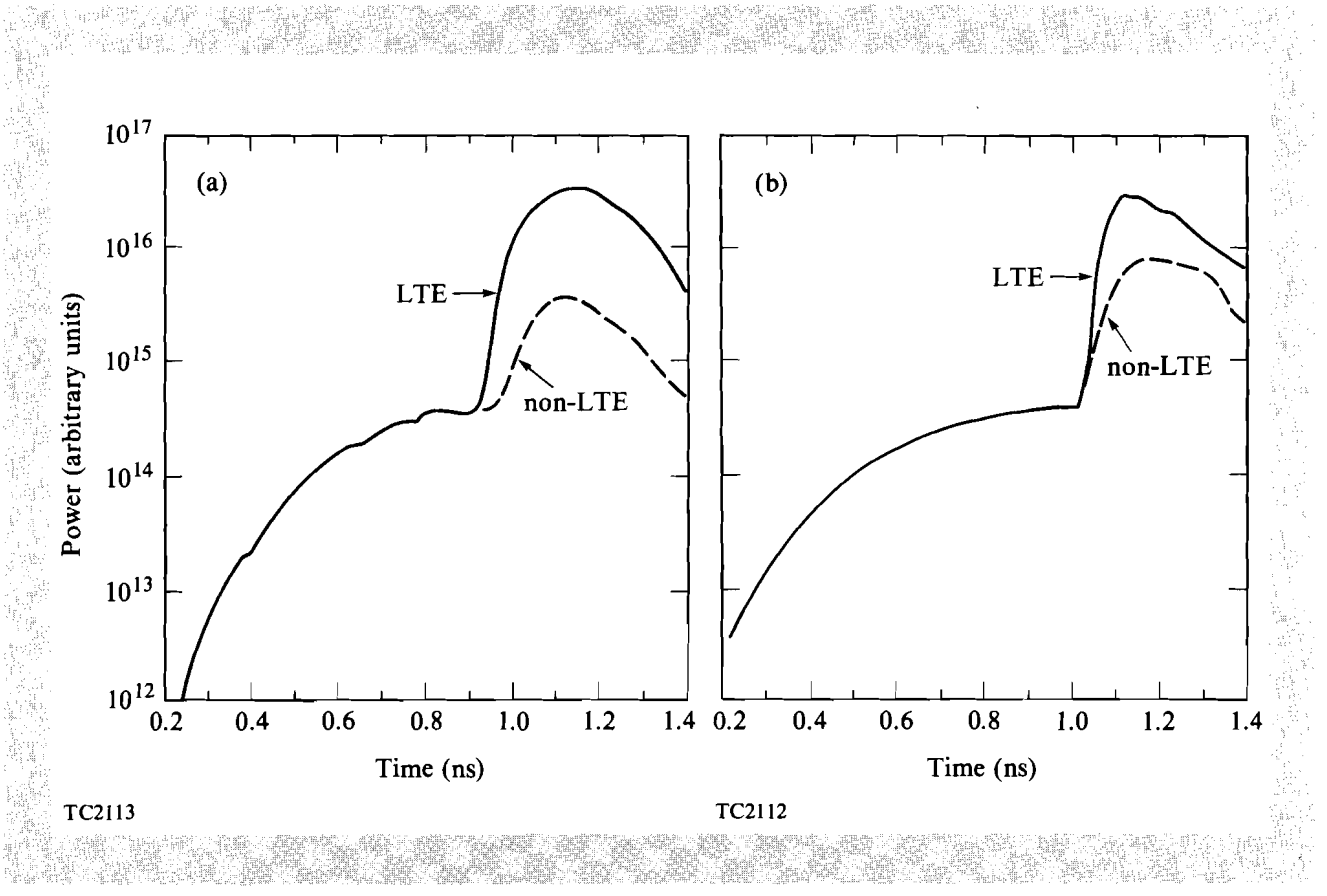

emission and a lack of line emission for marginal burn-through cases, such as 8 μm of CH at 3 $\times$ 10^{14} W/cm^2. The increase in rise time due to non-LTE is not large enough to explain the long rise times observed experimentally.

The aim of burn-through experiments is to measure the mass-ablation rate, which is an indication of the efficiency of the drive. The instantaneous mass-ablation rate is calculated[8] at the temporal midpoint between the onset of line emission at two plastic thicknesses using $\dot{m} = \rho\Delta d/\Delta t$, where ρ is the density of solid CH, Δd is the difference in the CH thicknesses, and Δt is the difference in onset time. If the target were uniformly illuminated, such an analysis would give the actual drive mass-ablation rate. But when the illumination contains high-intensity hot spots, burn-through measurements yield unreasonably large values for the mass-ablation rate because the onset time of the line emission corresponds to that of the high-intensity hot spots.[8] Therefore, while the absolute value of the measured mass-ablation rate reflects the level of nonuniformity, what is of interest is the scaling of the mass-ablation rate with absorbed intensity and how it compares with simulation. The mass-ablation rate is obtained from *LILAC* simulations by following the temporal excursion of the 500-eV isotherm (500 eV is approximately the temperature required for Si Hβ line emission). In this case, the same expression is used for calculating the mass-ablation rate except that now, Δd is the excursion of the 500-eV isotherm during the interval Δt. Several sets of mass-ablation rates are plotted against the absorbed intensity in Fig. 29.7. The discrete points are the instantaneous mass-ablation rate as calculated from the onset of line emission from experiment (solid symbols), from the weighted-average analysis (open symbols with cross), and from simulations at 3 I_0 (open symbols). The squares were obtained from the series at 3 $\times$ 10^{14} W/cm^2 and the circles from the series at 1 $\times$ 10^{15} W/cm^2. The solid line describes the computed mass-ablation rate from the 500-eV isotherm excursion from simulation at 3 I_0. The

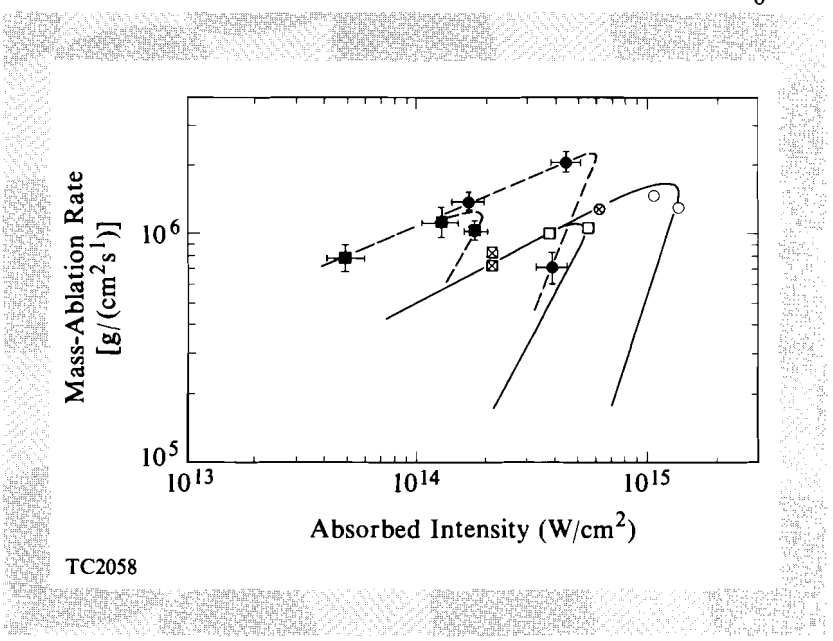

Fig. 29.7
Comparison between the instantaneous mass-ablation rate from experiment and simulation. The solid line is obtained from the excursion of the 500-eV isotherm in simulations at 3 I_0. The points are calculated from the onset times of the Si Hβ line; the dashed lines have been added for clarity. Squares are at 3 $\times$ 10^{14} W/cm^2 and circles at 1 $\times$ 10^{15} W/cm^2; solid: experiment; open: simulation at 3 I_0; cross: simulation, weighted average.

dashed line has been added to show how the discrete points belong to two sets of instantaneous mass-ablation-rate curves that parallel the set of simulation curves. On these curves, the peak of the pulse occurs in the middle of the "elbow." For the experimental points, the absorbed intensity was obtained from code simulation at nominal intensity.

The two experimental points on the downside of the dash curve confirm the rapid decrease of the mass-ablation rate, which had been predicted to occur after the peak of the pulse.[8] A scaling of the mass-ablation rate with absorbed intensity was obtained from the rising dash line: $\dot{m} \propto I^{0.43}$; the solid curve shows a slightly different scaling from simulation: $\dot{m} \propto I^{0.53}$. These scaling laws, but not the magnitude, are in reasonable agreement with those derived in Ref. 6 from charge collector data. Both the scaling and the magnitude of the mass-ablation rate are comparable to those obtained in the six-beam experiments.[8] Since the weighted-average points at 3×10^{14} W/cm^2 bracket the peak of the pulse and are very close, their value must be near to the maximum value of the weighted-average mass-ablation rate; this maximum mass-ablation rate is about two thirds of the measured value. Only the mass-ablation rate obtained from simulations at 3 I_0 approaches the experimental value; even there, the peak values from simulation are slightly lower than the measured values.

Summary

Transport experiments were carried out on the 24-beam OMEGA laser system at 351 nm. The laser beams were focused on spherical signature targets (glass balls or thick glass shells coated with CH) in such a way as to maximize the illumination uniformity. The temporal progress of the heat front was measured absolutely with the time-resolved x-ray spectrometer SPEAXS. Simulations of the experiment were carried out by taking account of the nonuniformity of the laser illumination on the target surface. The 24-beam illumination was characterized by superposing the ETP intensity distribution from one beam of OMEGA over the target surface. Weighted-average temporal profile of the line emissions was calculated from *LILAC* simulations at the intensities characterizing the intensity distribution on target. Inclusion of the nonuniformity advanced the onset time of the Si Hβ line by about 100 ps over the time calculated with the nominal intensity. But this advance in onset time was not sufficient to obtain agreement with the measured onset time. Increasing the value of the flux limiter from 0.06 to 0.1 made little difference at 3×10^{14} W/cm^2 and not enough at 1×10^{15} W/cm^2. The simulation intensities had to be increased to 3 I_0 for the onset times to agree with the experiment, suggesting that significant energy (a few percent) must exist at intensities equal to or larger than three times nominal.

The results of the transport experiment and their interpretation, using simulations that included the effects of illumination nonuniformity, lead to the following conclusions:

1. The effects of illumination nonuniformity cannot be neglected in the interpretation of transport experiments in which the progress of the heat front is measured spectroscopically, both in the time-resolved and time-integrated modes. Since the onset of

x-ray line emission or the burn-through depth can be affected by varying either the flux limiter or the laser intensity distribution on target, a full knowledge of the laser intensity distribution at the target surface would be required to pin down the value of the flux limiter using burn-through diagnostics. If the presence of illumination nonuniformity were neglected, a larger value of the flux limiter would be inferred than if illumination nonuniformity were taken into account.

2. The steep falloff of the scaling of the mass-ablation rate with absorbed intensity, observed in *LILAC* simulations,[8] has been confirmed experimentally. This result indicates that a single scaling cannot be used throughout the laser pulse in the interpretation of time-integrated measurements.

3. In the present experiments, the effect of non-LTE is small; it retards the onset of the x-ray line emission by at most 50 ps and increases slightly the rise time of that emission.

4. To obtain estimates of the mass-ablation rate in the presence of illumination nonuniformity, it is necessary to use diagnostics that are sensitive to the integrated or averaged intensity distribution on target. Such diagnostics include measurements of the ion blowoff distribution and of the implosion time. X-ray diagnostics of burn-through will be a useful diagnostics when the illumination uniformity is improved (for example, through the use of better optics or of incoherent illumination) or with the use of targets with high-Z dots imbedded in the plastic ablator (assuming that the intensity hot spots are not smaller than the dots).

5. X-ray diagnostics of targets with signature layers turn out to be good diagnostics of the illumination uniformity.

ACKNOWLEDGMENT

This experiment was part of a joint series of experiments with the Lawrence Berkeley National Laboratory, the Los Alamos National Laboratory, and the University of Maryland. The work at the University of Rochester was supported by the U.S. Department of Energy Office of Inertial Fusion under agreement No. DE-FC08-85DP40200 and by the Laser Fusion Feasibility Project at the Laboratory for Laser Energetics, which has the following sponsors: Empire State Electric Energy Research Corporation, General Electric Company, New York State Energy Research and Development Authority, Ontario Hydro, and the University of Rochester. Such support does not imply endorsement of the content by any of the above parties.

REFERENCES

1. J. Nuckolls, L. Wood, A. Thiessen, and G. Zimmerman, *Nature* **239**, 139 (1972).

2. T. J. Goldsack, J. D. Kilkenny, B. J. MacGowan, P. F. Cunningham, C. L. S. Lewis, M. H. Key, and P. T. Rumsby, *Phys. Fluids* **25**, 1634 (1982).

3. J. A. Tarvin, W. B. Fechner, J. T. Larsen, P. D. Rockett, and D. C. Slater, *Phys. Rev. Lett.* **51**, 1355 (1983).

4. B. Yaakobi *et al.*, *Phys. Fluids* **27**, 516 (1984).

5. A. Hauer *et al.*, *Phys. Rev. Lett.* **53**, 2563 (1984).

6. B. Yaakobi *et al.*, *J. Appl. Phys.* **57**, 4354 (1985).

7. R. C. Malone, R. L. McCrory, and R. L. Morse, *Phys. Rev. Lett.* **34**, 721 (1975).

8. P. A. Jaanimagi, J. Delettrez, B. L. Henke, and M. C. Richardson, *Phys. Rev. A* **34**, 1322 (1986).

9. S. Skupsky and K. Lee, *J. Appl. Phys.* **54**, 3662 (1983).

10. S. E. Bodner, *J. Fusion Energy* **1**, 221 (1981); J. H. Gardner and S. E. Bodner, *Phys. Rev. Lett.* **47**, 1137 (1981).

11. J. M. Soures, R. J. Hutchison, S. D. Jacobs, L. D. Lund, R. L. McCrory, and M. C. Richardson, in the *Proceedings of the Tenth Symposium on Fusion Engineering*, Philadelphia, PA (1983), p. 1392.

12. M. C. Richardson, P. W. McKenty, F. J. Marshall, C. P. Verdon, J. M. Soures, R. L. McCrory, O. Barnouin, R. S. Craxton, J. Delettrez, R. L. Hutchison, P. A. Jaaminagi, R. Keck, T. Kessler, H. Kim, S. A. Letzring, D. M. Roback, W. Seka, S. Skupsky, B. Yaakobi, and S. M. Lane, in *Laser Interaction and Related Plasma Phenomena Vol. 7,* edited by H. Hora and G. Miley (Plenum Press, New York, 1986).

13. B. L. Henke and P. A. Jaanimagi, *Rev. Sci. Instrum.* **54**, 1311 (1983).

14. P. A. Jaanimagi, L. DaSilva, G. G. Gregory, C. Hestdalen, C. D. Kiikka, R. Kotmel, and M. C. Richardson, *Rev. Sci. Instrum.* **57**, 2189 (1986).

15. An earlier version of *LILAC* is described in Laboratory for Laser Energetics Report No. 16 (1976).

16. A. B. Langdon, *Phys. Rev. Lett.* **44**, 575 (1980).

17. W. F. Huebner, A. L. Merts, N. H. Magee, and M. F. Argo, Los Alamos Report No. LA-6760 (1977).

18. Recent simulations, in which a non-LTE atomic physics model was included directly into *LILAC* (rather than as a postprocessor), showed little difference in the progress of the heat front in CH when compared to LTE results.

19. R. Epstein, S. Skupsky, and J. Delettrez, *J. Quant. Spectrosc. Radiat. Transfer* **35**, 131 (1986).

20. M. C. Richardson, S. Skupsky, J. Kelly, L. Iwan, R. Hutchison, R. Keck, R. L. McCrory, and J. M. Soures, *Proceedings of the 1983 Los Alamos Conference on Optics* (SPIE, Bellingham, WA, 1983), Vol. 380, p. 473.

1.B High-Resolution XUV Spectroscopy Using the OMEGA Laser

Introduction

For the past several years, the National Laser Users Facility (NLUF) has supported a research program in extreme ultraviolet (XUV) spectroscopy in cooperation with the Naval Research Laboratory (NRL) and the NASA Goddard Space Flight Center (GSFC). A 3-m grazing incidence spectrograph, originally built[1] as a rocket flight instrument at GSFC, was installed on the OMEGA target chamber. This instrument has been used to record spectra in the wavelength range 6 Å to 350 Å from a wide variety of targets.

High-resolution XUV spectroscopy is of fundamental interest for several reasons. The measured wavelengths can be used to derive the energy level structures and ionization potentials of highly charged ions. Trends along the isoelectronic sequences indicate the importance of relativistic and quantum electrodynamic (QED) effects, and deviations from expected results point the way toward improvements in the understanding of the atomic physics of highly charged ions. By comparing the experimental results with values calculated by atomic physics computer programs (such as those developed by Cowan, Grant, or Klapisch), the limitations in the present theoretical treatments of highly charged ions can be determined, and improvements can be made that result in more accurate calculated atomic data.

High-resolution XUV spectroscopy also contributes to the understanding of the plasma properties of laser-fusion targets. Different spectral lines are emitted from different plasma regions. The XUV lines are emitted from the hot corona and are characteristic of the electron temperature and density in the ablation plasma. Lines emitted from the central core will be characteristic of the density and temperature in that region. Line profiles and line shifts are powerful measures of the velocity fields in the plasma. Spectral lines from layered targets can be used to infer burn-through and electron energy transport in the corona.

Extreme ultraviolet spectroscopy has recently been used to identify energy levels of importance to x-ray laser systems and to observe population inversions on transitions in highly charged ions in linear laser-produced plasmas. These results represent progress toward the development of a soft x-ray laser with a wavelength below the carbon absorption edge at 43 Å.

XUV Spectroscopy

Figure 29.8 shows a schematic of the apparatus. A cylindrical mirror focuses the radiation from the target onto the entrance slit of the spectrograph. The linear image formed by the mirror is crossed at a small angle with the entrance slit, and this provides spatial resolution of the target in one dimension.[2] Shown in Fig. 29.9 is a typical XUV spectrum from copper-coated targets routinely used for beam pointing and focusing characterization. The 24 OMEGA beams were focused to

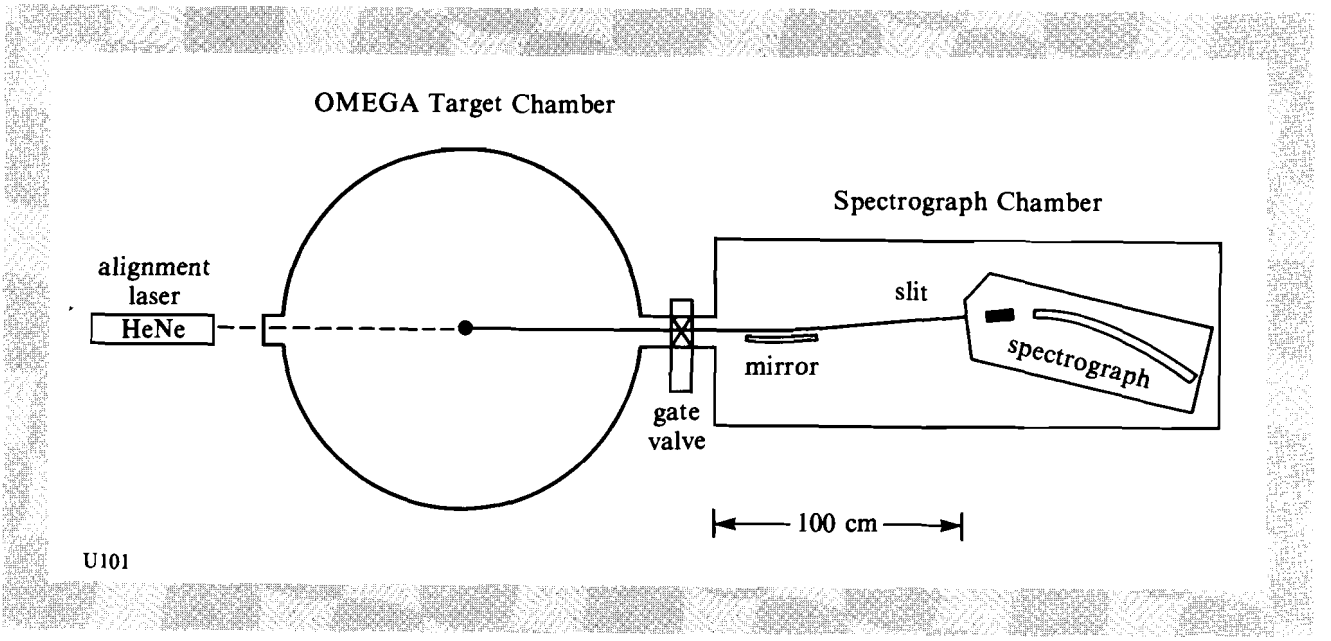

Fig. 29.8
Schematic of the apparatus showing the 3-m grazing incidence spectrograph, the cylindrical mirror, and the OMEGA target chamber.

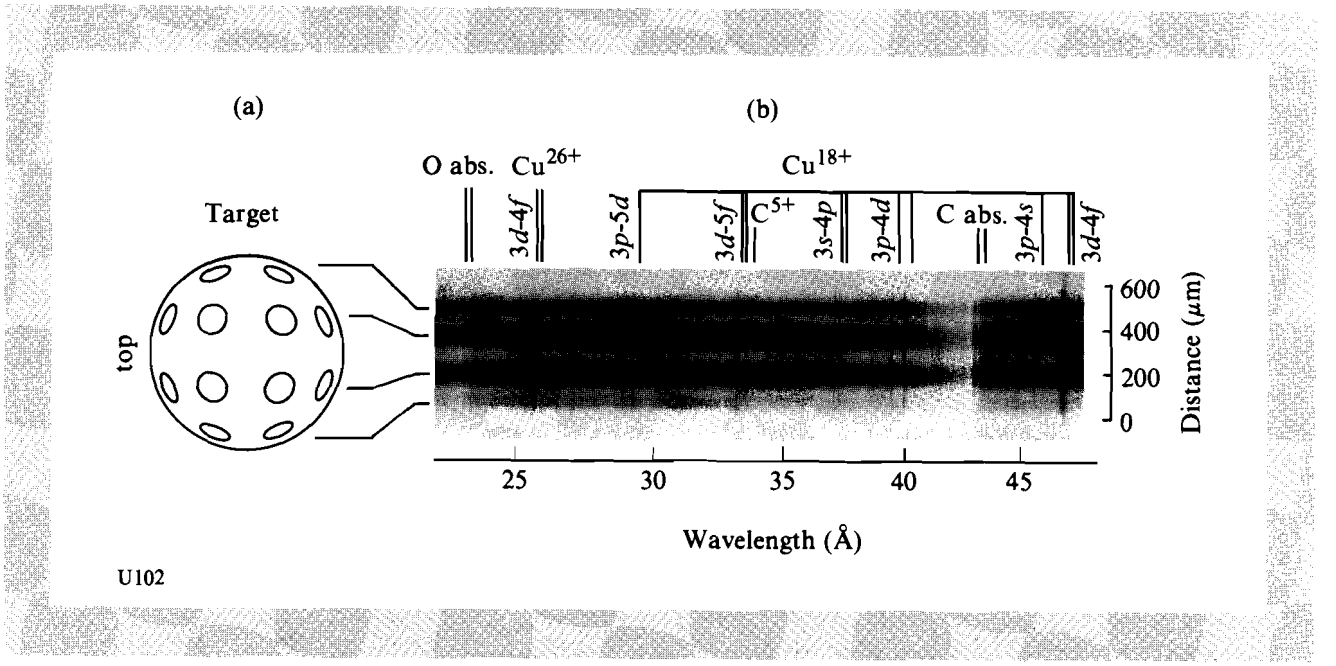

Fig. 29.9
(a) The pattern of laser focal spots on the hemisphere of the target facing the spectrograph. The diameter of each focal spot is 50 μm, and the diameter of the copper-coated target is 600 μm.
(b) The spectrum from 22 Å to 48 Å showing the $3d$-$4f$ transitions in Li-like Cu^{26+} near 25.6 Å, the n = 3-4 and n = 3-5 transitions in Na-like Cu^{18+}, and the C^{5+} Lyman-α transition at 33.736 Å. The carbon and oxygen inner-shell absorption features are present at 43.5 Å and 23.3 Å, respectively. The distance across the target is indicated by the scale at the right end of the spectrum.

50-μm spots in a spherically symmetric pattern, and the rows of focal spots were resolved in the XUV spectrum. Highly charged ions were abundant in the hot plasma, and spectral lines from these ions appear bright on the photographic plate in the laser focal regions. Transitions in Li-like through F-like copper were identified in the spectrum.[3,4] Such a hot copper plasma had never before been observed in the XUV region, and all of the Li-like Cu^{26+} transitions and many of the other copper transitions represent new identifications. This illustrates the uniqueness of the OMEGA facility for high-resolution XUV spectroscopy. No other laboratory presently has a high-resolution XUV spectrograph recording data from targets irradiated by such an intense laser.

The spectroscopy work supported by NLUF has resulted in 15 papers during 1985-86.[2-16] This work is summarized in Table 29.I. Elements from silicon [atomic number (Z) = 14] to uranium (Z = 92) have been studied. Transitions in the isoelectric sequences HI through NaI were identified in the elements $Z \leq 50$. For the heavier elements

Table 29.I
Table of elements and ionization stages that have been studied. The numbers refer to the references.

Element	Atomic Number	Isoelectronic Sequence													
		H	He	Li	Be	B	C	N	O	F	Na	Fe	Co	Cu	Zn
Si	14	8	8	8	8										
Cu	29			3	3	4	4	4	4	9					
Zn	30						9	9	9	9					
Ga	31						9	9	9	9					
Ge	32						9	9	9	9					
As	33								10	10					
Se	34								10	10	11				
Br	35					12	12	12	10	10	12				
Rb	37								10	10					
Y	39								13						
Zr	40								13	14					
Nb	41								13	14					
Mo	42									14					
Ru	44									14	15				
Rh	45									14	15				
Ag	47									14	15				
Cd	48									14	15				
Sn	50									14	15				
Sm	62											16	16		
Eu	63											16	16		
Gd	64											16	16		
Au	79											5	5	5	5
Pb	82											5	5	5	5
Bi	83											5	5	5	5
Th	90													5	5
U	92												5	5	5

U107

$Z \geq 62$, transitions in the FeI through ZnI isoelectronic sequences have been identified. Since the relativistic and QED contributions to the transition energies grow rapidly with increasing Z, the heavier elements are of particular interest for the study of these effects. The importance of QED effects in the CuI sequence is illustrated in Fig. 29.10. The inclusion of QED terms of order Z^4 in the calculated wavelengths improves the agreement with the observed wavelengths, but the growing discrepancies at high Z indicate that terms of higher order in Z should be included in the calculation.[5]

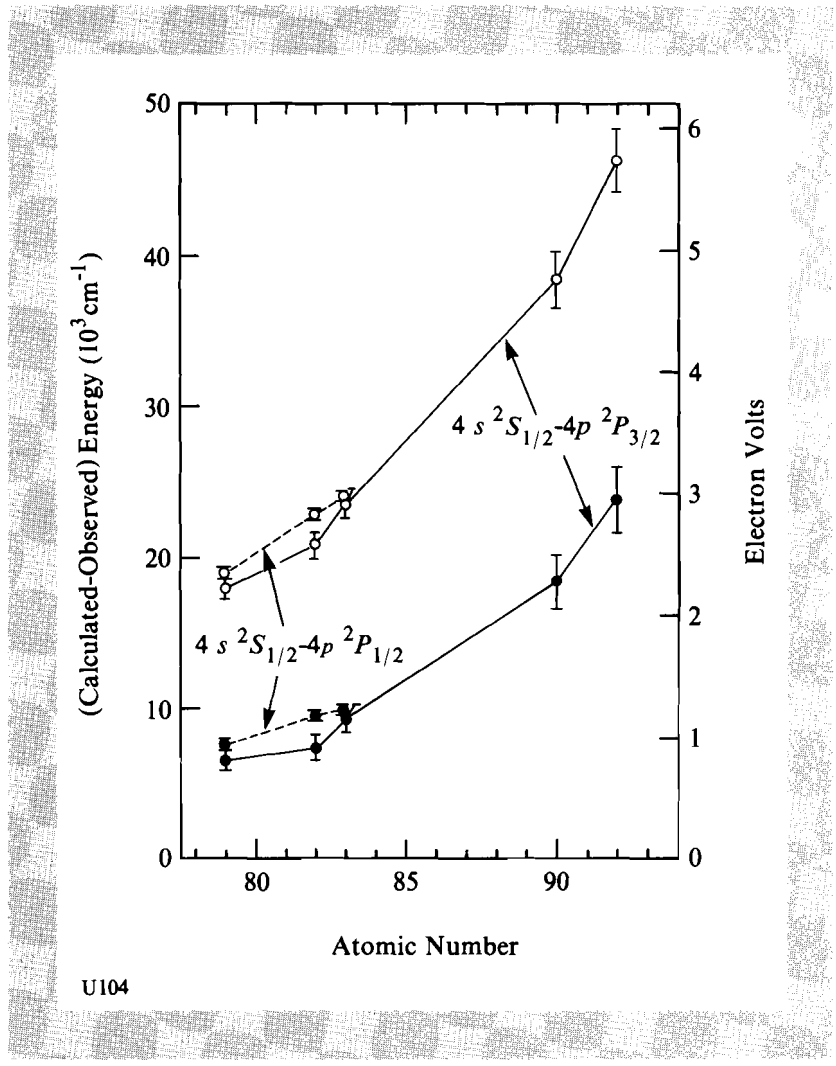

Fig. 29.10
Comparison of the observed energies of the 4*s*-4*p* transitions of Cu-like ions with the energies calculated by using Grant's program without QED contributions (open circles) and with QED contributions (solid circles).

Coronal Physics

The emission of XUV radiation is a function of the electron temperature and density of the corona. Depending primarily on the ionization potentials of the various ionization stages of a given element, different ionization stages are abundant at different electron temperatures. The spectral line intensities in a particular ion may also be sensitive to the electron temperature and density. For example, the ratio of the $3s\ ^2S_{1/2} - 3p\ ^2P_{3/2}$ and $3p\ ^2P_{3/2} - 3d\ ^2D_{5/2}$ transitions in Na-like ions is a strong function of electron density. Based on the measured intensity ratio for these transitions in Mo^{+31}, we determined

that the emission occurred in a plasma region with electron density of order 10^{21} cm^{-3}. The electron temperature was determined to be 2 keV to 3 keV.[6] In related experiments on layered targets, the observation of transitions from the underlying layers is characteristic of the burn-through time and electron energy transport in the corona.[17]

X-Ray Laser Research

The verification of population inversion and gain in the XUV and soft x-ray spectral regions has received considerable attention in the past several years. High-resolution spectroscopy is important for the identification of the lasing transitions and for the diagnosis of the gain medium. Following the results from Lawrence Livermore National Laboratory (LLNL)[18] on lasing in Ne-like selenium (Z = 34) at 206 Å and 209 Å, experiments were performed on selenium-coated Formvar at LLE. Up to eight OMEGA beams were focused in a line 100-μm wide and up to 13.6-mm long. Spectroscopic data from the selenium/Formvar plasmas were recorded on a number of shots.

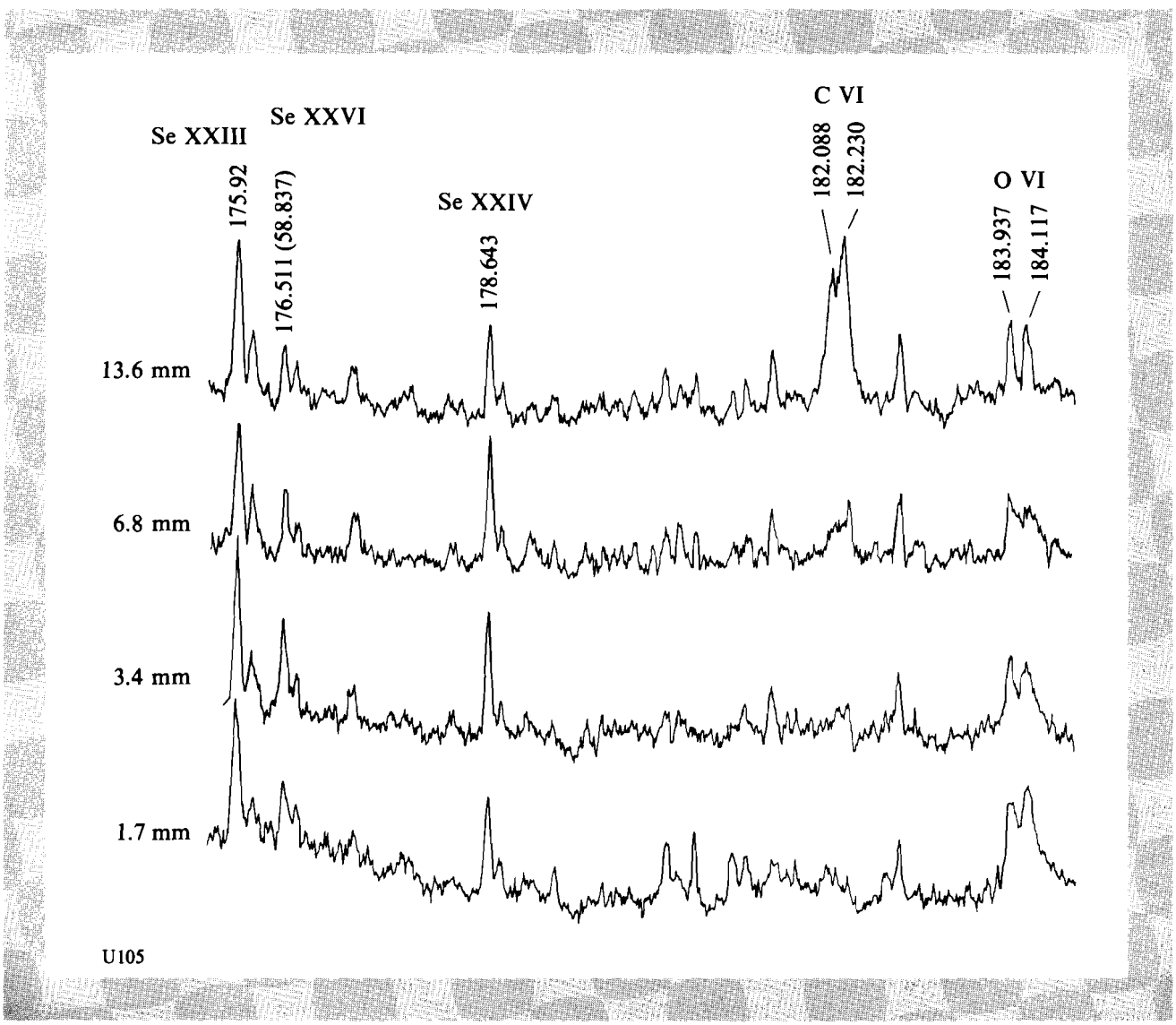

Fig. 29.11
The spectra from selenium/Formvar plasmas of lengths 1.7, 3.4, 6.8, and 13.6 mm. The intensity of the C^{5+} n = 3-2 feature at 182 Å increases dramatically with the length of the plasma. This is consistent with a gain of 3 cm^{-1}.

Although none of the selenium transitions indicated gain, the hydrogenic C^{5+} $n = 3$-2 transitions at 182 Å increased dramatically in intensity when the length of the plasma was increased, as shown in Fig. 29.11.[7] This was consistent with a gain on these transitions of 3 cm^{-1}. Modeling indicates that the mechanism producing the population inversion was radiation cooling of the plasma by the highly charged selenium ions, collisional recombination, and cascading into the C^{5+} $n = 3$ level.[19]

One of the primary motivations in x-ray laser research is to produce coherent radiation at wavelengths below the carbon absorption edge at 43 Å. When a biological specimen is irradiated with such radiation, contrast is enhanced by the increased absorption in the organic material. The $\Delta n = 0$ transitions, such as the $3s-3p$ transitions in Ne-like selenium, scale slowly to lower wavelengths with increasing Z, while the wavelengths of the $\Delta n = 1$ transitions in hydrogenic ions scale rapidly as Z^{-2}. In order to produce gain at wavelengths below 43 Å in laboratory plasmas, it is advantageous to use transitions in hydrogenic ions. The $n = 2$-3 and $n = 2$-4 transitions in H-like and He-like silicon fall in the wavelength range 24 Å-40 Å and are of interest for lasing below the carbon absorption edge. As shown in Fig. 29.12, these transitions were identified for the first time in the XUV spectra from glass microballoons.[8]

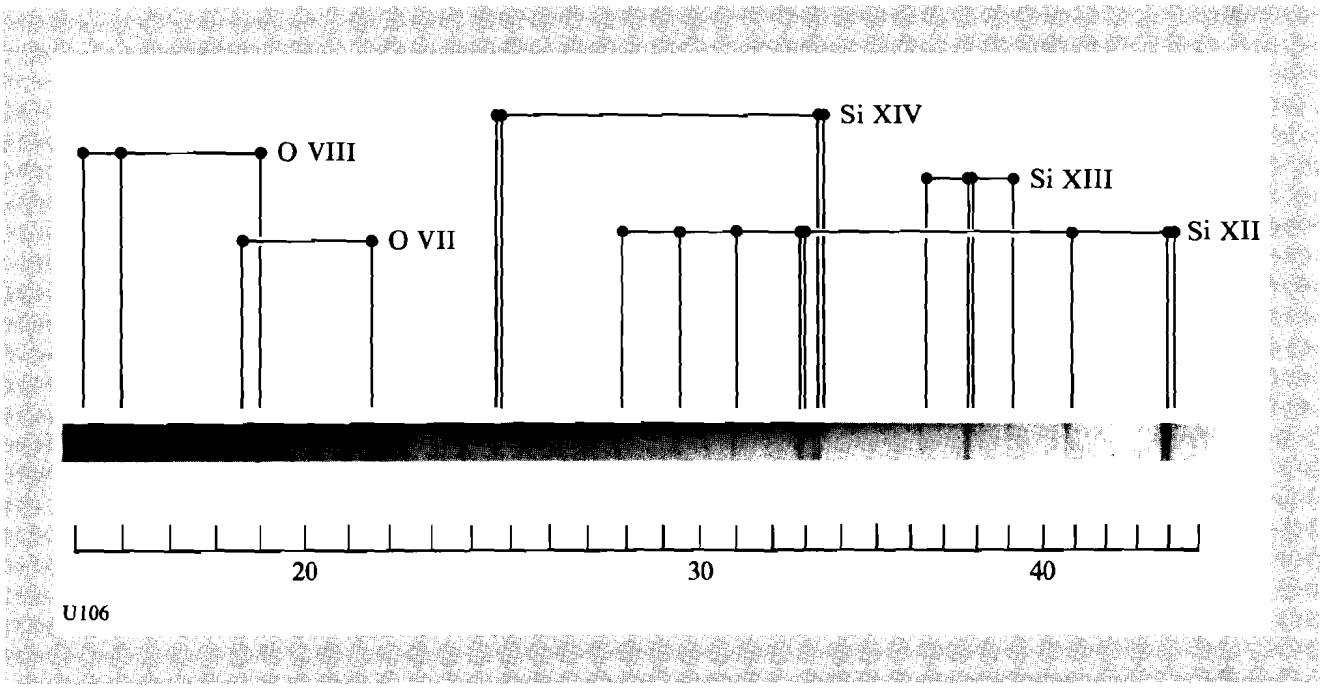

Fig. 29.12
XUV spectrum from a glass microballoon between 15 Å and 45 Å. Transitions in highly ionized silicon and oxygen are indicated.

Ions with one electron outside closed shells have energy-level structures similar to hydrogenic ions, and transitions in Li-like, Na-like, and Cu-like ions also scale rapidly to lower wavelengths with increasing Z. In point-focus experiments performed at LLE, population inversions have been observed on transitions in a number of highly charged "one-electron" ions. For example, population inversion in Li-like Cu^{26+} on the $3d$-$4fd$ transitions at 26 Å was observed in the experiments previously mentioned.[3] Li-like ions have great promise

for achieving gain in this interesting wavelength region, and future experiments are planned.

Summary

The XUV spectroscopy research supported by NLUF has been a productive collaboration with the Naval Research Laboratory and the NASA Goddard Space Flight Center. High-resolution spectroscopy has produced understanding of relativistic and QED effects in highly charged ions of elements with a high atomic number. The electron density and temperature of the coronal plasma have been determined. Progress has been made in x-ray laser research with the observation of gain on the C^{5+} 182-Å transitions and the observation of population inversion in Li-like Cu^{26+} at 26 Å.

Plans for the future include the implementation of a normal-incidence XUV spectroheliograph and a 2-m grazing incidence Schwob-Fraenkel spectrograph with a microchannel plate intensifier. The spectroheliograph images the XUV radiation emitted from the coronal plasma of the laser-irradiated target, which is useful for understanding coronal physics. The spectroheliograph has been installed on the OMEGA target chamber, and preliminary data look promising. The design of this instrument is similar to instruments built by NRL and flown on the spacecraft Skylab. These instruments recorded high-quality images of the solar corona that even now represent the best data of this kind on the solar corona.

ACKNOWLEDGMENT

This work was supported by the U.S. Department of Energy Office of Inertial Fusion. The research and materials incorporated in this work were partially developed at the National Laser Users Facility at the University of Rochester's Laboratory for Laser Energetics, with financial support from the U.S. Department of Energy under agreement No. DE-FC08-85DP40200.

REFERENCES

1. W. E. Behring, R. J. Ugiansky, and U. Feldman, *Appl. Optics* **12**, 528 (1973).
2. W. E. Behring, C. M. Brown, U. Feldman, J. F. Seely, J. Underwood, M. C. Richardson, and F. J. Marshall, *J. Opt. Soc. Am. B* (to be published).
3. C. M. Brown, J. O. Ekberg, U. Feldman, J. F. Seely, M. C. Richardson, F. J. Marshall, and W. E. Behring, *J. Opt. Soc. Am. B* (to be published).
4. J. O. Ekberg, J. F. Seely, C. M. Brown, U. Feldman, M. C. Richardson, and W. E. Behring, *J. Opt. Soc. Am. B* (to be published).
5. J. F. Seely, J. O. Ekberg, C. M. Brown, U. Feldman, W. E. Behring, J. Reader, and M. C. Richardson, *Phys. Rev. Lett.* (to be published).
6. S. Goldsmith, J. F. Seely, U. Feldman, W. E. Behring, and L. Cohen, *J. Appl. Phys.* **58**, 4011 (1985).
7. J. F. Seely, C. M. Brown, U. Feldman, M. Richardson, B. Yaakobi, and W. E. Behring, *Opt. Commun.* **54**, 289 (1985).

Section 2
ADVANCED TECHNOLOGY DEVELOPMENTS

2.A The Study of Shock Launching in Silicon Using Pulsed X-Ray Diffraction

The laser generation of shocks encompasses a wide range of physical processes and effects, since virtually every property of condensed matter can be altered with pressure. Particular areas of scientific study in which laser-generated shocks may find application include energetic materials,[1] high-velocity impacts,[2] and the alteration of the materials properties of certain alloys and ceramics.[3] For the more conventional shock drivers, the shock-launching region – i.e., the initial layer of the material of interest from which the shock begins – is obscured by the driving mechanism. Also, the timing of diagnostic apparatus is not readily accomplished on the subnanosecond time scale necessary to directly observe the launching of a shock wave into a lattice. For this reason, well-resolved experimental studies of the shock-launching region up to now have been intractable. Laser-driven shocks do not present this limitation.

We report results of an experiment in which we probed the initial few (4 to 5) microns of the shock-launching region in silicon with pulsed x rays, and directly measured the temporal variation of lattice spacing by Bragg x-ray diffractometry. We have also examined the experimentally determined peak density as a function of laser irradiance.

The use of x rays to measure the density of shocked materials was first performed by Johnson and co-workers in the early 1970s.[4] They shocked LiF to several hundred kilobars using conventional explosive

techniques,[5,6] and diffracted a 40-ns to 50-ns pulse of x rays[7] off the shocked material. To our knowledge, however, the work presented here, with a five-hundred-fold improvement in temporal resolution, is the first of a similar nature to be presented since then, and the first time that the launch region has been studied in detail.

The experiment was performed on the JANUS research laser system at the Lawrence Livermore National Laboratory (LLNL). The experimental setup is shown in schematic form in Fig. 29.13. The shocked targets consisted of 250-μm-thick (111) silicon wafers 5 cm in diameter, the surface of which had been coated first with 1000 Å of aluminum and then with 25 μm of parylene (CH). The motivation for such a target design is explained below. Half of the target was irradiated in a vacuum by a 1 ± 0.05-ns pulse of 1.06-μm laser light, at an irradiance varying from 0.8 J cm^{-2} to 8 J cm^{-2} with an on-target beam diameter of 3.9 cm. A beam block prevented irradiation of the other half of the target; diffraction from this unshocked region gave us a reference point from which to measure the changes in Bragg angle. After the shock had been launched in the silicon crystal, a second laser beam containing ~ 10 J of 0.53-μm light in 100 ps, which was synchronous with known and variable delay with respect to the shock-launching beam, was focused to a ~ 40-μm-diameter spot on a second, calcium-containing target. The ionized He-like calcium x-ray lines thus produced[8] were Bragg diffracted off the silicon and recorded on Kodak DEF x-ray film. The reduction in x-ray intensity due to passage through the 25-μm plastic overcoat is estimated to be $\sim 35\%$, with a further $\sim 4\%$ reduction due to passage through the aluminum. A single laser shot provided recordable x-ray levels; a series of shots was taken to obtain data at different irradiances and delay times.

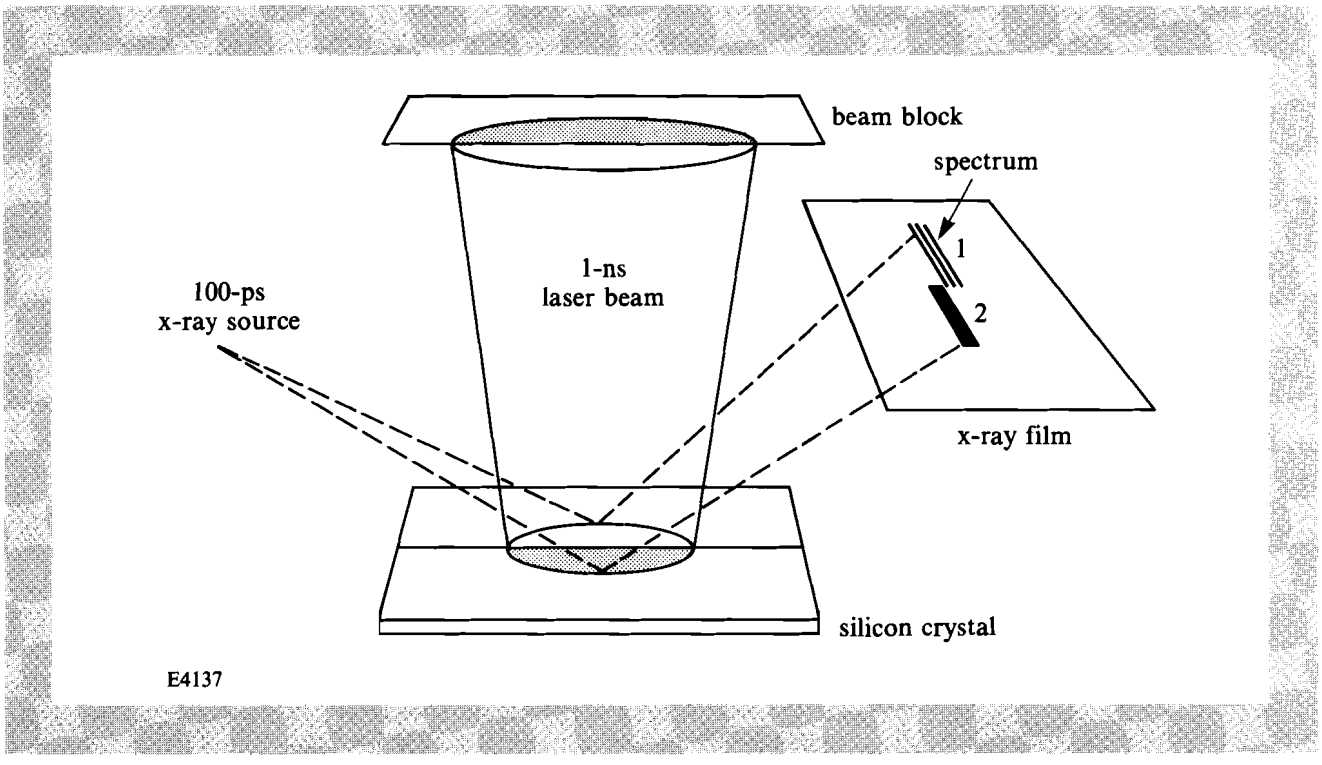

Fig. 29.13
The experimental setup showing schematically the x-ray diffraction from the unshocked (1) and shocked (2) crystal.

Previous experiments at irradiances similar to those used here have shown that uncoated silicon is simply heated by the laser light rather than shocked,[9] due to the several-millimeter absorption length of 1.06-μm light in silicon at room temperature. The aluminum coating was therefore applied to act as an abrupt absorber to the incident radiation. This effectively prevented the penetration of the laser light into the silicon, and instead produced an aluminum plasma that in turn generates a pressure pulse for driving the shock into the material. Overcoating the aluminum with plastic transparent to 1.06-μm light causes the expanding aluminum plasma to be inertially confined between silicon and plastic, which in turn increases the strength of the shock launched into the silicon. Such overcoating techniques have previously been used to enhance shock pressures in the tens-of-kilobar range.[10]

A set of typical diffraction patterns is shown in Fig. 29.14. The three lines in the unshocked region are the resonance line (3.177 Å), the intercombination line (3.193 Å), and the unresolved j, k dielectronic satellites (3.21 Å) of He-like calcium.[8] In the shocked region of the crystal, the lattice spacing d is reduced, increasing the diffraction angle θ in accordance with a differentiation of Bragg's law:

$$\Delta(2d)/2d = -\cot\theta\,\Delta\theta.$$

This effect can clearly be seen in Fig. 29.14. A simple measurement of the maximum angular shift thus gives us a direct measurement of the peak density, and knowledge of the distribution of angular shifts yields information on the distribution of lattice spacings within the probed region.

The probe depth of the x rays in such highly strained crystals is determined by the photoelectric absorption coefficient rather than the extinction length. This is because x rays incident at a particular angle only diffract off that particular region of the crystal at which the lattice spacing is such that the Bragg condition is satisfied; the rest of the crystal up to that point (with slightly different lattice spacings) simply acts as an x-ray filter. A Beer's law attenuation factor of $1/e$ for the He-like calcium lines in silicon corresponds to an x-ray path length of 8.5 μm, or a depth of 4.3 μm below the surface at the Bragg angle. Taking further account of the signal dynamic range, we estimate a probe depth of 4 μm to 5 μm below the surface.

Diffraction measurements such as those shown in Fig. 29.14 were made for a variety of levels of irradiance and delay times. We define the laser beam delay as the interval between the arrival, at chamber center, of the peak of the long (shock-producing) pulse followed by the peak of the short (x-ray-producing) pulse. The x-ray probe delay was 0.09 ns greater than the delay between laser beams, due to the setup geometry and time-of-flight considerations. It can be seen from Fig. 29.14 that at 0.0-ns delay we still observe diffraction at the original Bragg angle as well as diffraction over a range of angles, corresponding to a range of lattice spacings up to a peak compression of 3.35%. The obvious physical explanation for this is that, at this

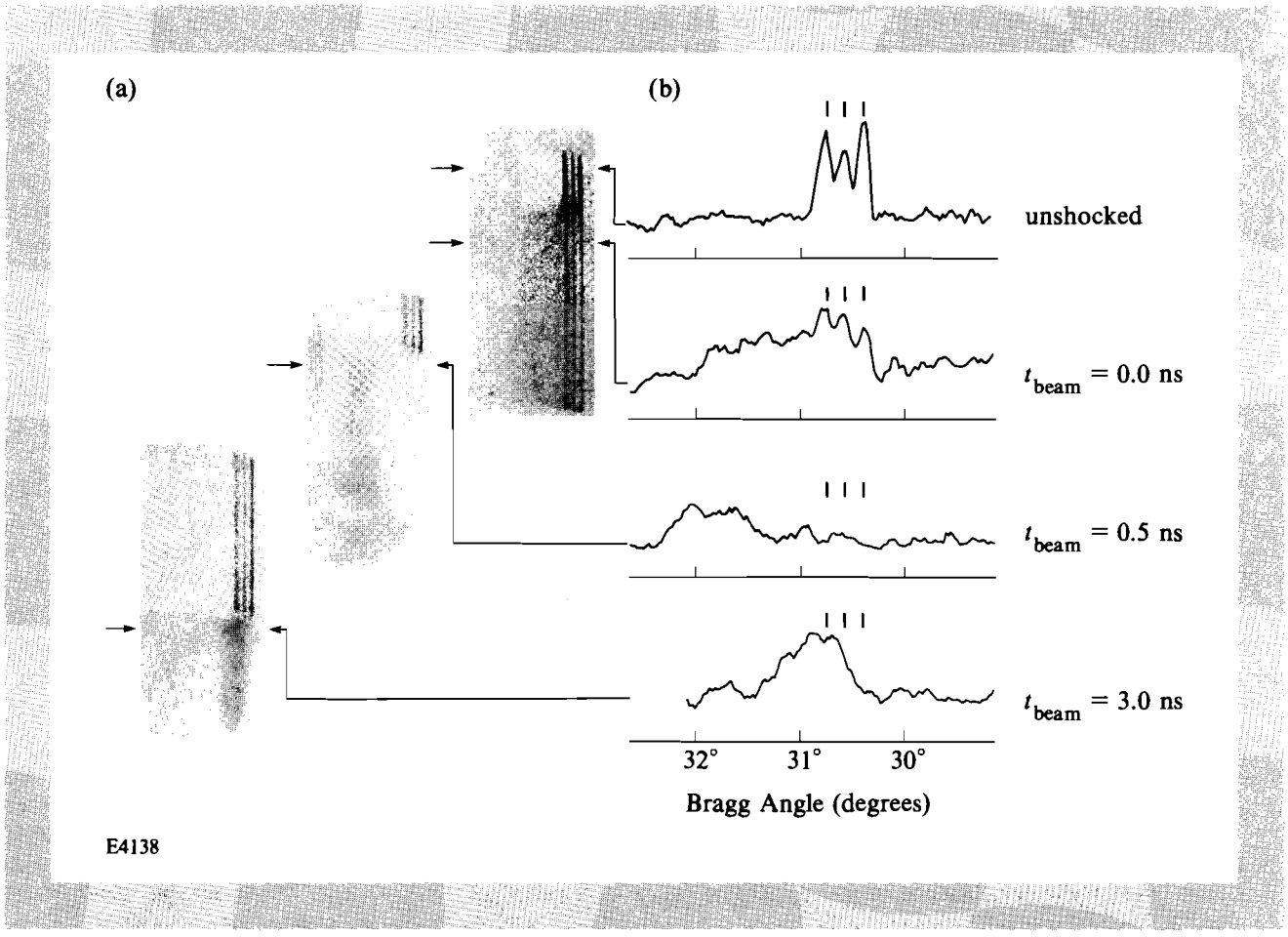

Fig. 29.14
Diffraction results.
(a) X-ray line spectra diffracted from silicon shocked at an incident-energy density of 4 ± 0.3 J cm^{-2} (an irradiance of 4×10^9 W cm^{-2}) are shown adjacent to reference lines simultaneously diffracted by the unstrained silicon lattice, from a series of beam delays. Each photograph represents a separate shot and beam delay.
(b) Densitometer scans, taken at indicated locations through the spectra in (a), are shown for a typical unshocked spectrum, and shocked spectra at 0.0-ns, 0.5-ns, and 3.0-ns beam delays.

early time, the shock has not yet penetrated past the maximum probe depth, and we are probing through the shock front into the as-yet-unshocked region. For all data collected after this delay time, when the shock has proceeded further into the material, we no longer observe diffraction from the unperturbed crystal.

In Fig. 29.15 we show the peak change in interatomic spacing as a function of time for those shots where the average energy density of the shock-producing laser pulse was 4 ± 0.3 J cm^{-2} on target (i.e., an average irradiance of 4×10^9 W cm^{-2}). The accuracy of the laser timing may include a constant systematic error estimated to be no more than ± 200 ps; random timing fluctuations were evidently of lesser magnitude. The error bar on the density measurement results primarily from a consideration of observed effects of laser nonuniformities on the maximum Bragg diffraction angle. [These

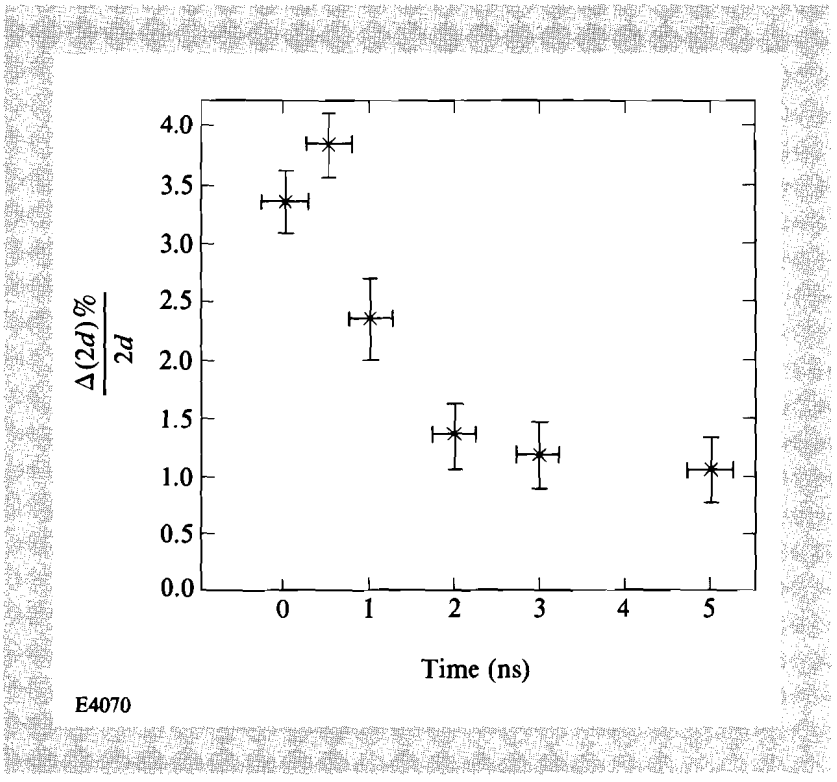

Fig. 29.15
The measured peak change in interatomic spacing as a function of time for those laser shots with an energy density of 4 ± 0.3 J cm^{-2}.

effects can be seen in Fig. 29.14(a) as a variation in angular shift in the diffracted radiation.] Other effects, such as intrinsic x-ray line width, crystal rocking curve breadth, and x-ray source broadening, are of considerably lesser importance. A maximum change of the lattice spacing of 3.85% was observed at this energy density, and the data are consistent with a pressure pulse with a FWHM of 1 ns. It can be seen that the rise time of the shock compression is similar to that of the laser pulse. However, after peak compression has been reached, the density falls off with a far longer decay time than that of the laser. Indeed, even 5 ns after the peak of the shock-producing pulse, the crystal is still compressed by $\sim 1\%$. At no time did we observe the front-surface density to fall below that of solid. Such inhibition of the rarefaction wave has previously been observed by other diagnostic methods[11] (using similar tamped targets), and is due to the tamping effect of the plastic.

The Hugoniot elastic limit (HEL) has been reported to occur in (111) silicon at a compression of 2.6%,[12,13] corresponding to a pressure of about 54 kbar. Applying the stress-volume curve of Gust and Royce[12] to the observed 3.85% compression, we estimate a peak stress of 67 kbar at an energy density of 4 J cm^{-2}. However, in comparing these results to Hugoniot measurements, it should be borne in mind that we are probing the shock-launching phase, rather than merely observing the arrival of an already steepened shock front. Furthermore, elastic response may extend above the HEL on a transient basis.[14,15]

Figure 29.16 shows the experimentally measured peak compressions as a function of irradiance for various probe delay times. The rapid

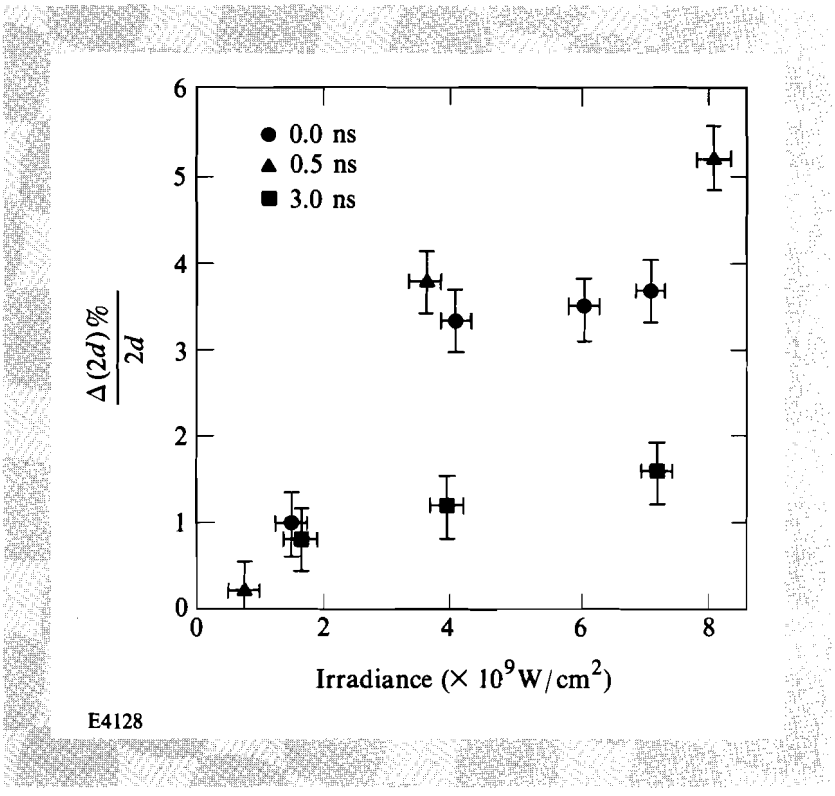

Fig. 29.16
The peak change in interatomic spacing as a function of irradiance for delay times indicated. The HEL is at 2.6% compression.

falloff in compression at low irradiances is due to the increased importance of thermal conduction into the silicon at lower irradiances,[11] as well as an increase in the fraction of laser energy expended in the latent heat of vaporization of the aluminum.

The technique of pulsed x-ray diffraction from laser-shocked materials opens up several new avenues for the study of the transient response of crystal lattices. For instance, while we have shown here that it is possible to measure the density on the front surface of a shocked crystal, the technique can obviously also be applied to the rear surface. Because the x rays can probe through the crystal, we can in principle observe a shock wave before, during, and after arrival at a free surface, making density measurements at any stage for any sample thick enough to diffract. The temporal resolution afforded by this technique, coupled with its ability to probe crystal structure, may allow us to time-resolve pressure-induced phase transitions, as well as study possible transient effects in crystals compressed beyond the HEL.[14,15] Furthermore, a detailed study of the x-ray reflectivity as a function of angle may yield density-depth information, using methods similar to those developed for studying laser-annealed crystals.[16,17]

Significant advances have recently been achieved in the uniformity with which pulsed lasers can irradiate a target,[18] which we anticipate may lead to a major improvement in the uniformity of laser-generated shocks. Such improvement would enhance the precision of x-ray diffraction and a wide range of other measurements involving laser-generated shocks. Also of particular importance to x-ray probing is the advent, within the next few years, of laser pulses as short as 1 ps

capable of producing x rays with the intensities necessary for single-shot recording.[19,20]

In conclusion, we have directly observed the temporal history of density change within a laser-shocked crystal by short-pulse x-ray diffraction. We have observed diffraction from material both in front of and behind the developing shock front at early stages during the laser drive pulse. We have followed the lattice compression to values above the HEL, and further observed the onset of rarefaction as the pressure pulse decayed. Crystallinity was preserved throughout this process.

ACKNOWLEDGMENT

This work was supported by the U.S. Department of Energy Office of Inertial Fusion under agreement No. DE-FC08-85DP40200 and by the Laser Fusion Feasibility Project at the Laboratory for Laser Energetics, which has the following sponsors: Empire State Electric Energy Research Corporation, General Electric Company, New York State Energy Research and Development Authority, Ontario Hydro, and the University of Rochester. Such support does not imply endorsement of the content by any of the above parties.

Research was performed in collaboration with the U.S. Naval Research Laboratory and Los Alamos National Laboratory. The author acknowledges the assistance of the staff of the JANUS research laser system at the Lawrence Livermore National Laboratory.

REFERENCES

1. L. C. Yang, *J. Appl. Phys.* **45**, 2601 (1974).
2. A. N. Pirri, *Phys. Fluids* **20**, 221 (1977).
3. B. P. Fairand, B. A. Wilcox, W. J. Gallagher, and D. N. Williams, *J. Appl. Phys.* **43**, 3893 (1972).
4. Q. Johnson, A. Mitchell, R. N. Keeler, and L. Evans, *Phys. Rev. Lett.* **25**, 1099 (1970).
5. Q. Johnson, A. Mitchell, and L. Evans, *Nature* **231**, 310 (1971).
6. Q. Johnson, A. C. Mitchell, and L. Evans, *Appl. Phys. Lett.* **21**, 29 (1972).
7. Q. Johnson and A. C. Mitchell, *Phys. Rev. Lett.* **29**, 1369 (1972).
8. U. Feldman, G. A. Doschek, D. J. Nagel, R. D. Cowan, and R. R. Whitlock, *Astrophys. J.* **192**, 213 (1974).
9. J. G. Lunney, P. J. Dobson, J. D. Hares, S. D. Tabatabaei, and R. W. Eason, *Opt. Commun.* **58**, 269 (1986).
10. N. C. Anderholm, *Appl. Phys. Lett.* **16**, 113 (1970).
11. B. P. Fairand and A. H. Clauer, *J. Appl. Phys.* **50**, 1497 (1979).
12. W. H. Gust and E. B. Royce, *J. Appl. Phys.* **42**, 1897 (1971).
13. T. Goto, T. Sato, and Y. Syono, *Jpn. J. Appl. Phys.* **21**, L369 (1982).
14. J. R. Asay, G. R. Fowles, G. E. Duvall, M. H. Miles, and R. F. Tender, *J. Appl. Phys.* **43**, 2132 (1972).
15. Y. M. Gupta, G. E. Duvall, and G. R. Fowles, *J. Appl. Phys.* **46**, 532 (1975).

16. B. C. Larson, C. W. White, T. S. Noggle, J. F. Barhorst, and D. M. Mills, *Appl. Phys. Lett.* **42**, 282 (1983).

17. B. C. Larson and J. F. Barhorst, *J. Appl. Phys.* **51**, 3181 (1980).

18. R. H. Lehmberg and S. P. Obenschain, *Opt. Commun.* **46**, 27 (1983).

19. D. Strickland and G. Mourou, *Opt. Commun.* **56**, 219 (1985).

20. P. Maine, D. Strickland, and G. Mourou (private communication).

2.B Thermal Conductivity in Dielectric Thin Films

In 1984 Decker *et al.*[1] reported the measurement of thermal conductivity for freestanding thin films of SiO_2 and Al_2O_3. Values were found to be one to two orders of magnitude lower than those for the corresponding bulk materials. The authors attributed this difference to the unique microstructure of dielectric thin films (primarily columnar for vapor-deposited coatings[2]), which, along with defects and impurities, would be expected to reduce the phonon mean-free path, and thus the conductivity. Work by others has recently reinforced these findings for other dielectric coatings.[3,4]

Low thermal conductivity has important implications for electronic and optical applications, where heat deposited in a thin dielectric layer must be dissipated to prevent damage. Models that account for thermal transport in multilayer thin-film structures[5] may have no predictive value if they employ bulk conductivity data.

Most techniques used to measure the thermal conductivity of dielectric materials in thin-film form are difficult and time consuming. This article describes a method developed at LLE[6] that is relatively rapid, nondestructive, and capable of evaluating samples in a conventional film-on-substrate geometry. The technique has the additional advantage of being able to study the thermal barriers created at interfaces between the coating and the substrate. We show preliminary data that suggest thermal conductivity varies considerably among dielectric coating materials.

Our thermal conductivity apparatus is shown schematically in Fig. 29.17. It consists of an environmentally isolated sample chamber, a control and readout module, and a data processor. The sample stage and control module were purchased in 1975[7] to perform conductivity measurements on bulk materials. The thermal comparator technique for determining bulk thermal conductivity has been extensively described by R. W. Powell.[8,9] The commercial unit was converted into a high-precision device by controlling the temperature of both the samples and sample stage, and by averaging the signal of the output data.

The principle of operation and the calibration procedure for the apparatus are shown in Fig. 29.18. After placing a test sample on the

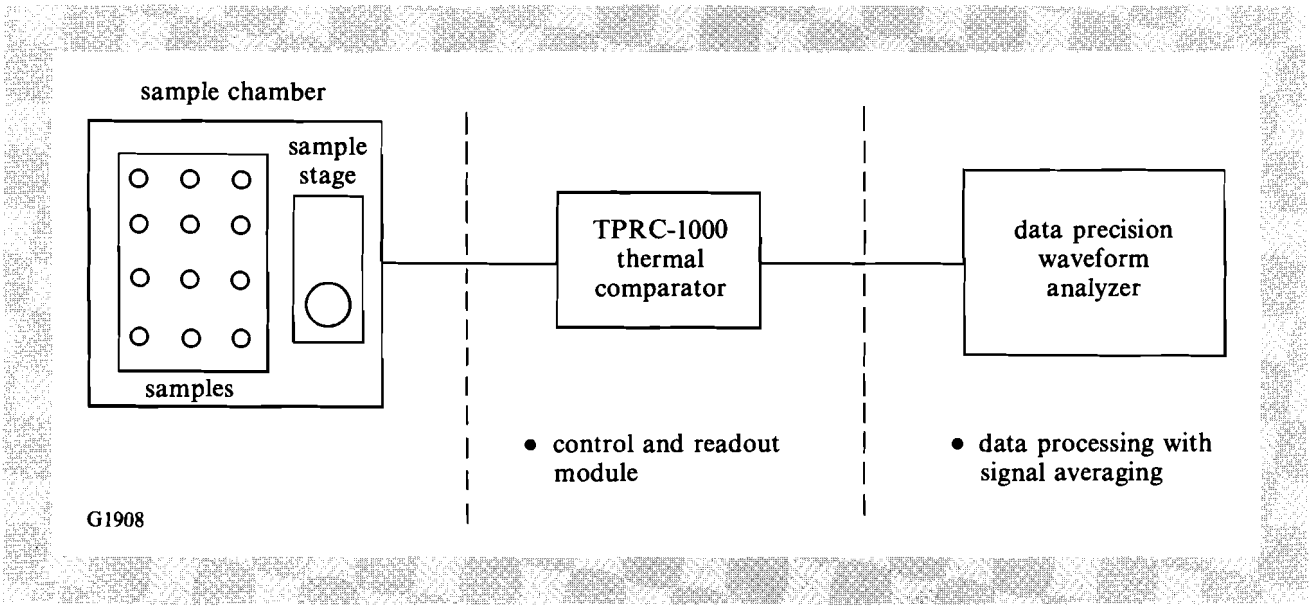

Fig. 29.17
High-precision thermal comparator apparatus. Samples and sample stage are contained in a sealed environmental chamber in which temperature is controlled to $\pm 0.1°C$, and humidity is kept constant at 6% $\pm 1\%$. A data precision waveform analyzer is used to acquire millivolt signals from the comparator readout module. The thermal comparator apparatus has been substantially modified from the commercial unit purchased in 1975.

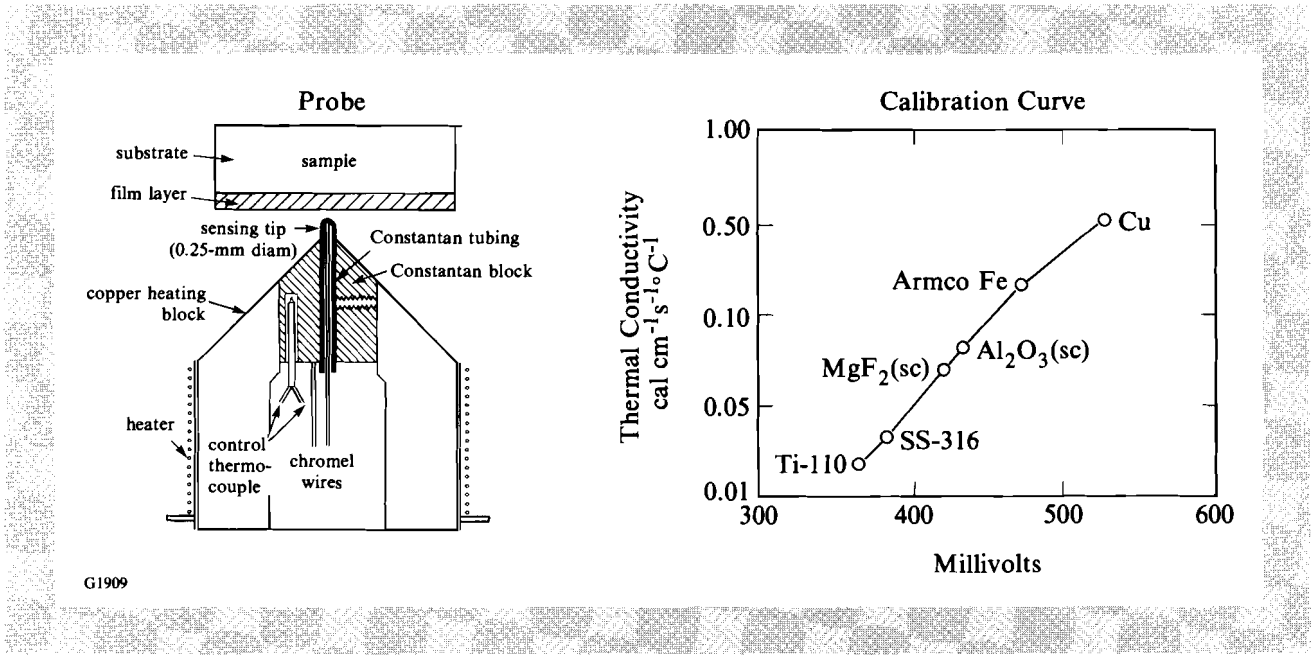

Fig. 29.18
Principle of operation. The tip of the heated thermocouple probe (56°C) is cooled when contacted to the coated substrate (36°C). A voltage generated between the probe junction and an internal, heated control junction reaches a steady-state value and is recorded. Thermal conductivity is determined by comparing calibration standard signals with unknowns. The thin-film coating causes a reduction in the conductivity of the substrate material.

sample stage, a thermocouple junction sensing tip is raised into contact with the sample surface. Heat flows from the hot tip (56°C to 66°C) to the cooler sample (36°C), and in approximately 10 seconds a steady-state condition is established. A voltage, generated by the temperature difference between the sensing tip and a reference junction, is acquired by the control module and displayed as a function of time on a waveform analyzer. Bulk solids of known conductivity are used to generate a thermal conductivity calibration curve (see Fig. 29.18), and unknowns are compared to these standards.

A highly conductive material, such as single-crystal silicon, is an optimum substrate for studying the conductivity of dielectric thin films. When a coated-silicon part is evaluated, the lower conductivity of the thin-film layer causes the substrate to register a reduced value of apparent conductivity. Measurements on a suitable set of coated substrates, in conjunction with a simple theoretical interpretation, provide a means for calculating the thermal conductivity of the thin-film material.

The model and assumptions for this work are illustrated in Fig. 29.19. We assume the heat flow to be perpendicular to all interfaces [see Fig. 29.19(a)]. The heat flux $\dot{Q}$ per unit area A from the probe tip into the sample is assumed constant through the thin film, any barrier layer, and the substrate. It is given as

$$\frac{\dot{Q}}{A} = \frac{k_f \Delta T_f}{h_f} = \frac{k_b \Delta T_b}{h_b} = \frac{k_s \Delta T_s}{h_s} \quad , \tag{1}$$

where we define the total temperature drop as

$$\Delta T_{\text{net}} \equiv \Delta T_f + \Delta T_b + \Delta T_s \, .$$

The absolute thicknesses and thermal conductivities of the thin-film/barrier layer/substrate combination are identified in Fig. 29.19(b). The net thermal conductivity of the combination k_{net} is then given by the relationship

$$\frac{\dot{Q}}{A} \equiv \frac{k_{\text{net}} \, \Delta T_{\text{net}}}{h_f + h_b + h_s} \quad ; \tag{2}$$

k_{net} is the quantity measured in our experiment. The thicknesses h_f and h_b of the film and any barrier layer are much less than the thickness of the substrate. By normalizing all thicknesses and conductivities in terms of the substrate thickness h_s and conductivity k_s we can derive the following relationship:

$$\frac{1}{K_{\text{net}}} = \left(\frac{1}{K_f} - 1\right) H_f + \left(\frac{1}{K_b} - 1\right) H_b + 1 \quad , \tag{3}$$

where $$K_{\text{net}} = \frac{k_{\text{net}}}{k_s} \, , \; H_f = \frac{h_f}{h_s} \, , \text{ etc.}$$

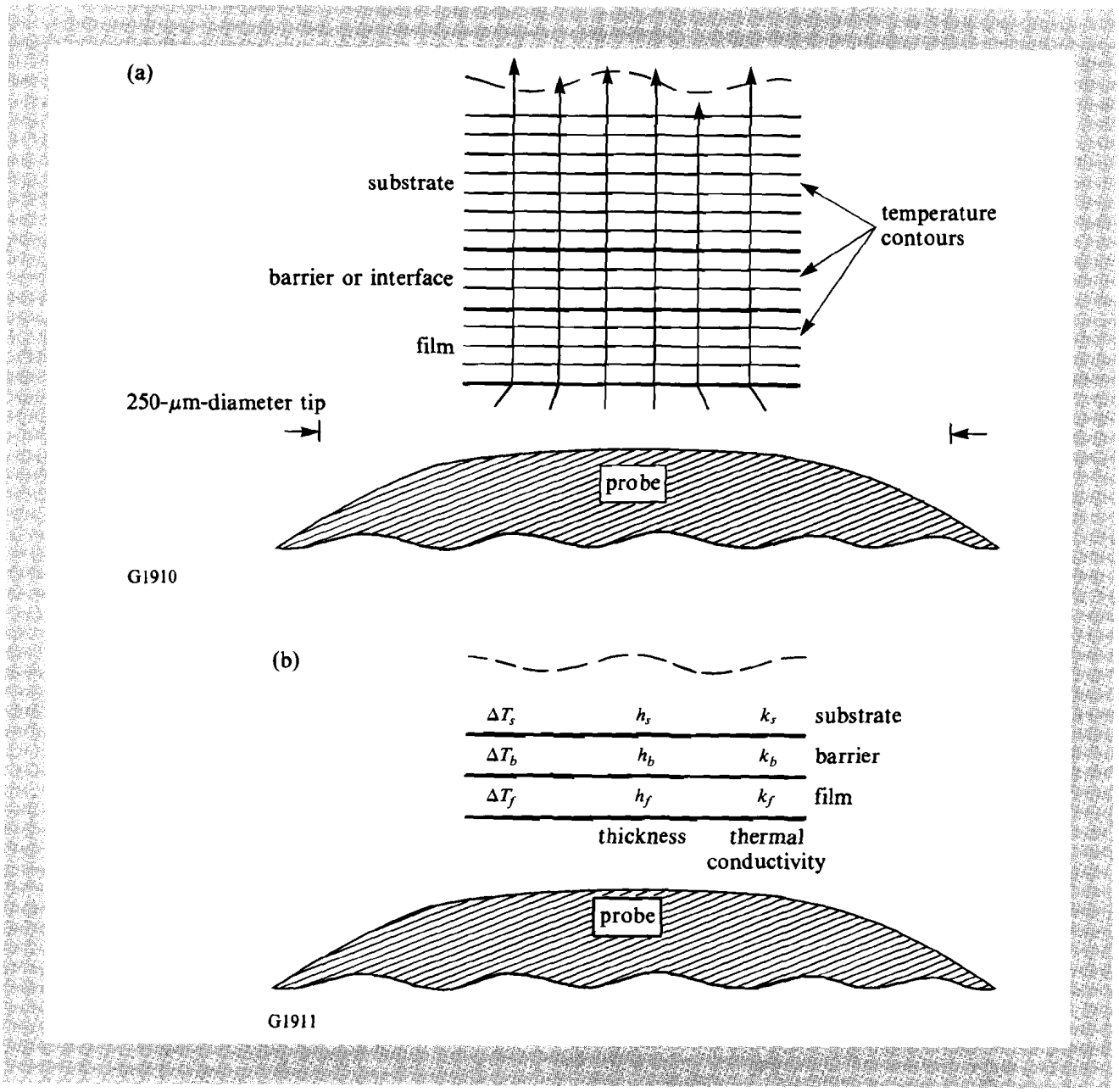

Fig. 29.19
Geometry and assumptions required to model experiment.
(a) The same heat flux $\dot{Q}$ is normal to the thin film, any barrier layer, and the substrate.
(b) The thicknesses and conductivities of the thin-film and barrier layers are normalized in terms of the substrate thickness and conductivity.

This is the equation for a straight line. By measuring the net conductivity k_{net} for a coating material deposited in different film thicknesses on a set of identical substrates, we can plot $1/K_{net}$ as a function of normalized film thickness H_f. The actual film conductivity k_f is derived from the slope of the straight line. The thermal conductivity of any barrier on interface layer k_b can be estimated from the zero thickness intercept of the line, providing reasonable assumptions concerning the barrier layer thickness h_b are made.

For experimental validation of our theory and approach, we examined single films of SiO_2 and Al_2O_3, deposited on single-crystal silicon substrates with a (111) surface orientation. The substrates were disc shaped, with dimensions of 50-mm diameter by 5-mm thickness. Their surfaces were 80/50 scratch/dig, ten fringes flat, and used as received from the vendor.[10] The coating depositions were carried out in our thin-film coating facility in a chamber equipped for *e*-beam evaporation. Single rotation was employed, substrate temperature was held at 200°C, and the O_2 partial pressure was 3×10^{-5} Torr during deposition. Materials were evaporated at a rate of 10 Å/s. We chose to deposit four film thicknesses per evaporant using an incremental coat/remove technique. This meant that the chamber was vented to air to remove one part each time a desired thickness was achieved. Coating thicknesses were estimated to be 0.5, 1.0, 2.0, and 4.0 μm $\pm 10\%$, based upon the output of an optical thickness monitor.

The photograph in Fig. 29.20 shows the location of test samples within the controlled environment chamber, and the method employed for sample placement during a set of measurement runs. The experiment is performed with samples at a temperature of 36°C to minimize thermal gradients introduced by the operator. Once mounted on the sample stage, a part is loaded with a 0.5-kg weight to prevent lifting from the contact pressure of the probe tip. During a set of runs, up to ten parts, consisting of coating and calibration samples, are sequentially measured. The measurement sequence is repeated several times over one to two hours to allow for a calculation of net thermal conductivity with an error estimate representing the reproducibility of the measurement.

G1912

Fig. 29.20
Instrumentation for thermal conductivity studies. Measurements are performed with the enclosure temperature at 36°C to minimize operator-induced temperature fluctuations. Samples are mounted on the sample stage and loaded with a 0.5-kg weight to insure uniform contact pressure with the probe tip. A run is completed in one to two hours.

The data for single films of SiO_2 and Al_2O_3 on silicon are shown in Fig. 29.21, where the reciprocal of normalized net thermal conductivity ($1/K_{net}$) has been plotted as a function of normalized film-layer thickness. From the slopes we calculate the thermal conductivities of the two materials to be as follows:

$$SiO_2\text{: } k_f = 4 \times 10^{-5} \text{ cal cm}^{-1}\text{s}^{-1}\text{°C}^{-1}$$
$$Al_2O_3\text{: } k_f = 5 \times 10^{-5} \text{ cal cm}^{-1}\text{s}^{-1}\text{°C}^{-1} \quad , \qquad (4)$$

with standard deviation, $\sigma = 1 \times 10^{-5}$.

The two values are the same within the standard deviation of the measurement. Because the zero thickness intercept is not equal to 1, we can make the observation that some form of low-conductivity barrier layer exists between the SiO_2 or Al_2O_3 coatings and the Si substrate. This barrier layer may be related to the oxidation of the Si substrate, and, if we assume it to be of the order of 10 Å to 100 Å in thickness, then a simple calculation suggests that the conductivity of the barrier layer is in the range of $\sim 10^{-7}$ cal cm^{-1}sec^{-1}°C^{-1}.

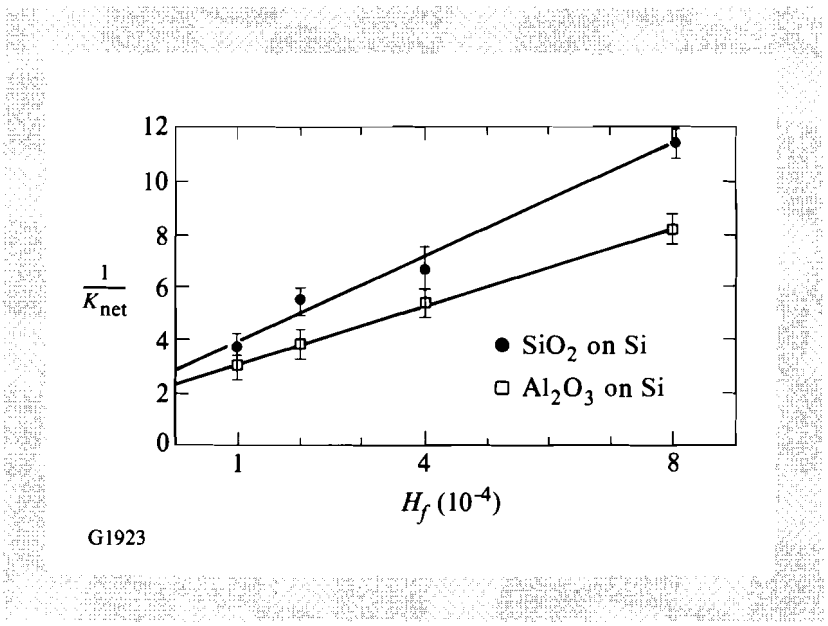

Fig. 29.21
Data for single films of SiO_2 and Al_2O_3 on silicon substrates. The reciprocal normalized net conductivity is plotted against normalized film thickness. Film conductivity is calculated from the slope of each line, and the effects of any barrier layers are related to the zero thickness intercept. Low conductivity is indicated (see text for details).

In a second experiment we examined single films of MgF_2 deposited on silicon, sapphire, and magnesium fluoride substrates. A description of the substrates is given in Table 29.II. The objectives of this experiment were to evaluate a fluoride film and to study substrate dependence.

The fluoride films were deposited under the same conditions as described above, except that the chamber was kept at its base pressure in the 10^{-6} Torr range. In addition, three separate coating runs were made to deposit each of three different film thicknesses on appropriate sets of substrates. The resulting thicknesses were measured with a Talystep surface profilometer and were found to be 0.6, 1.7, and 3.8 μm $\pm 5\%$.

Table 29.II
Substrate for MgF_2 single films

- Si
  - single crystal (111)
  - 45-mm diameter × 6-mm thickness
  - Polishing Corporation of America
- Al_2O_3
  - single crystal (*c*-axis 60° to face)
  - 25-mm diameter × 6-mm thickness
  - General Ruby and Sapphire Corp.
- MgF_2
  - single crystal (*c*-axis ⊥ to face)
  - 50-mm diameter × 5-mm thickness
  - Optovac, Inc.

G1962

Net conductivity measurements for the MgF_2 coatings on silicon were not reproducible. Close examination of the coatings showed tensile-stress fracture in films of all three thicknesses, and significant delamination was noted for the two thicker films after several weeks. We could obtain no useful information for this sample set.

The data for MgF_2 films on sapphire and magnesium fluoride substrates are shown in Fig. 29.22. The probe tip temperature was increased to 66°C for these measurements, which improved reproducibility by a factor of 2 compared to previously described results. No substrate dependence is observed, and from the zero slope we conclude that the film conductivity is essentially equal to that of the

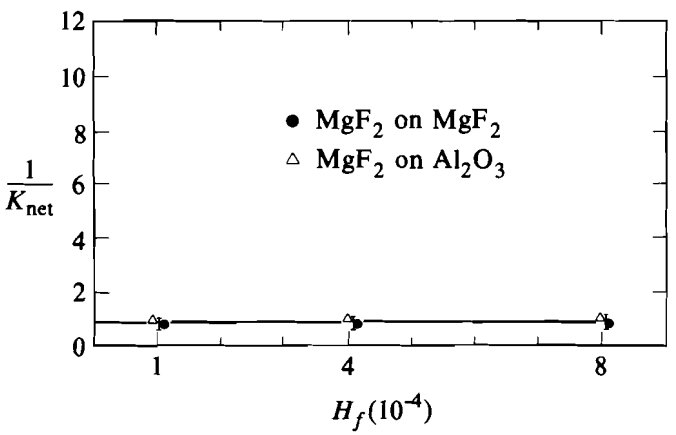

Fig. 29.22
Data for single films of MgF_2 on sapphire and magnesium fluoride substrates. The zero slope and unity intercept contrast sharply with the oxide film data in Fig. 29.21. High conductivity is indicated (see text for details).

substrates, which is 8×10^{-2} cal $cm^{-1}sec^{-1}°C^{-1}$. The microstructure of *e*-beam-deposited MgF_2 films is known to be polycrystalline,[11] whereas that of SiO_2 has been characterized as amorphous.[12] This may, in part, explain why the fluoride film conductivity compares favorably with the bulk and the oxide film data do not. The ordinate intercept at $1/K_{net} = 1$ indicates the absence of any barrier layer for these coating/substrate combinations, and this may be a result of the stability of sapphire and magnesium fluoride against oxidation.

Our results and those of two other groups[1,3] are compared on a logarithmic scale in Fig. 29.23. Values for single-crystal bulk solids Si, Al_2O_3, MgF_2, SiO_2, and fused silica are included for reference. We can make the following observations:

1. Oxide films exhibit thermal conductivities that are orders of magnitude below those of bulk solids.
2. One fluoride film, MgF_2, appears to exhibit a thermal conductivity representative of the bulk material.
3. A low-conductivity barrier layer exists for films deposited on single-crystal silicon, and it may be due to oxidation formed on the substrate surface prior to application of the oxide films.

In the future we will begin a thermal conductivity survey of dielectric coating materials, with special emphasis on ways to modify a given material's conductivity through the method of deposition. We will also extend the theory and experiment to multilayer structures.

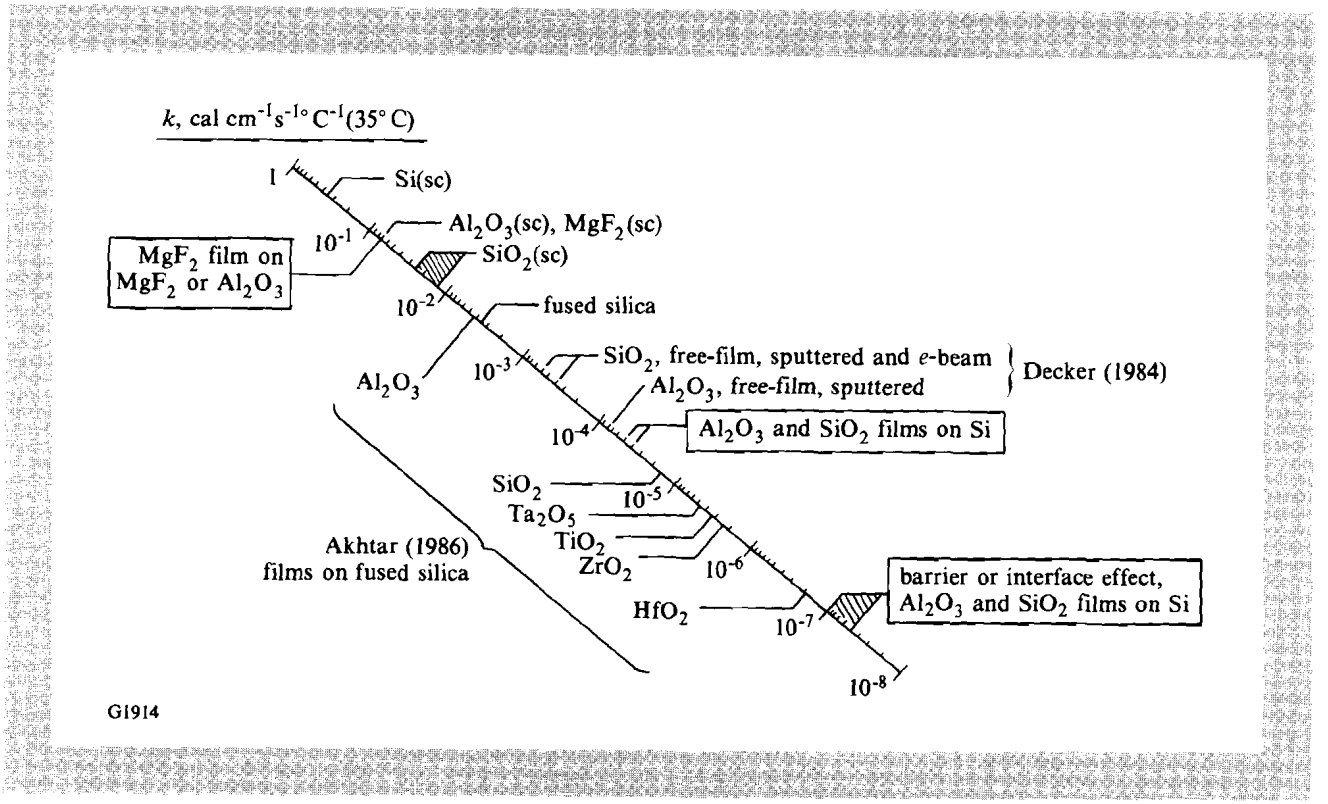

Fig. 29.23
Comparison of dielectric thin-film thermal conductivity results. Decker[1] *et al.* results are for freestanding oxide films; Akhtar[3] *et al.* results are for 1-μm-thick oxide films on fused-silica substrates.

ACKNOWLEDGMENT

This work was supported by the New York State Center for Advanced Optical Technology of The Institute of Optics, the U.S. Department of Energy Office of Inertial Fusion under agreement No. DE-FC08-85DP40200, and by the Laser Fusion Feasibility Project at the Laboratory for Laser Energetics, which has the following sponsors: Empire State Electric Energy Research Corporation, General Electric Company, New York State Energy Research and Development Authority, Ontario Hydro, and the University of Rochester. Such support does not imply endorsement of the content by any of the above parties.

REFERENCES

1. D. L. Decker, L. G. Koshigoe, and E. J. Ashley, *Nat. Bur. Stand. (U.S.), Spec. Publ.* **727**, 291–297 (1986).
2. See, for example, LLE Review **26**, 88–97 (1986); B. W. Krakauer, J. S. Gau, and D. J. Smith, *J. Mater. Sci. Lett.* **5**, 667–670 (1986).
3. S. M. J. Akhtar and D. Ristau, "Thermal Conductivity of Dielectric Films and Correlation to Damage Threshold at 1064 nm," presented at the 18th Annual Symposium on Optical Materials for High Power Lasers, Boulder, CO, 3–5 November 1986.
4. R. T. Swimm, "Photothermal Measurements of Optical Coating Thermal Transport Properties," presented at the 18th Annual Symposium on Optical Materials for High Power Lasers, Boulder, CO, 3–5 November 1986.
5. M. R. Lange, J. K. McIver, and A. H. Guenther, *Thin Solid Films* **125**, 143–155 (1985).
6. S. D. Jacobs, S. E. Gilman, D. G. Angeley, D. J. Smith, and J. C. Lambropoulos, "Thermal Conductivity in Dielectric Thin Films," presented at the Optical Society of America Annual Meeting, Seattle, WA, 20–24 October 1986.
7. TC-1000 Thermal Comparator, Lafayette Instrument Company, Lafayette, IN (no longer commercially available).
8. R. W. Powell, *J. Sci. Instrum.* **34**, 485–492 (1957).
9. R. W. Powell, in *Thermal Conductivity*, edited by R. P. Tye (Academic Press, London and New York, 1969), Vol. 2, Chap. 6, pp. 275–338.
10. Polishing Corporation of America, Santa Clara, CA.
11. H. K. Pulker and J. Maser, *Thin Solid Films* **59**, 65–76 (1979).
12. K. H. Guenther, *Appl. Opt.* **23**, 3806–3816 (1984).

Section 3
NATIONAL LASER USERS FACILITY NEWS

National Laser Users Facility (NLUF) activity during the first quarter of FY87 centered on an experiment that could be carried out while improved optics were being installed in the OMEGA laser, support for future user experiments, and preparing for FY88 proposals. Experiments of **Dr. J. G. Jernigan** from the Space Sciences Laboratory at the University of California, Berkeley, and **Prof. J. S. DeGroot** from the University of California, Davis, were supported during this quarter.

Dr. F. Marshall of LLE is collaborating with Dr. Jernigan on the development of a two-dimensional active readout array to replace film in an x-ray pinhole camera mounted on the OMEGA target chamber. Images were recorded with the 10 × 64 element PIN diode array and the data are now being analyzed.

Prof. DeGroot visited LLE on 10 November 1986 to talk to LLE personnel about upcoming plasma physics experiments on GDL and OMEGA. It was decided that the experiment to measure the wavelength scaling of ion acoustic decay instabilities will be done on both GDL and OMEGA. Experiments planned for OMEGA will require laser power densities of 3×10^{16} W/cm^2 incident onto both glass and CH spherical targets. This high-power density is needed to study the ion acoustic decay instability. Instrumentation for this experiment is being installed on the OMEGA target chamber.

The Steering Committee to review the FY88 proposals has been approved by DOE. Its members include

Dr. Dwight Duston	OSD/SDIO;
Dr. Peter Eisenberger	EXXON Research and Engineering Co.;
Dr. Damon Giovanielli	Los Alamos National Laboratory;
Dr. William Kruer	Lawrence Livermore National Laboratory;
Dr. David Nagel	Naval Research Laboratory; and
Prof. Ravindra Sudan	Cornell University.

The Steering Committee will be chaired by **Provost Brian Thompson** of the University of Rochester. There are 11 FY88 proposals for the committee to review and evaluate.

For more information regarding proposal guidelines and the resources available at the National Laser Users Facility, please contact:

Manager
National Laser Users Facility
Laboratory for Laser Energetics
University of Rochester
250 East River Road
Rochester, New York 14623-1299
(716) 275-2074

ACKNOWLEDGMENT

This work was supported by the U.S. Department of Energy Office of Inertial Fusion under agreement No. DE-FC08-85DP40200.

Section 4
LASER SYSTEM REPORT

4.A GDL Facility Report

GDL continued operation this quarter as a target interaction facility. A number of shots were devoted to interaction experiments. Damage-testing shots for the materials group have resulted in the successful tests of liquid-crystal waveplates, which will improve polarization control over existing liquid-crystal polarizers. The ALPHA (25th beam for OMEGA) beam has been successfully aligned, tuned, and activated.

A summary of GDL operations for this quarter follows:

Pointing/Alignment Shots	65
Beamline Test and Activation	65
Damage Testing	7
ALPHA Test Shots	36
ALPHA/OMEGA Synchronized Shots	2
Target Shots	149
TOTAL	324

4.B OMEGA Facility Report

During the first quarter of FY87, OMEGA activities included continuation of the laser system modifications begun during the previous quarter. The main objective of the modifications was the improvement of beam quality and diagnostics.

The driver-line reconfiguration is concluded. The driver seed beam to the OMEGA beamline splitters has near-perfect circularity, a controllable beam profile, and less than a one-tenth wave of total aberration in the beam.

A new beam diagnostic, which consists of a charge-injection-device (CID) camera coupled to an image-processing computer, has provided shot-to-shot capability for on-shot centering ($\pm 1\%$) and beam profile diagnostics to the driver line. A typical reduction of the camera data is shown in Fig. 29.24.

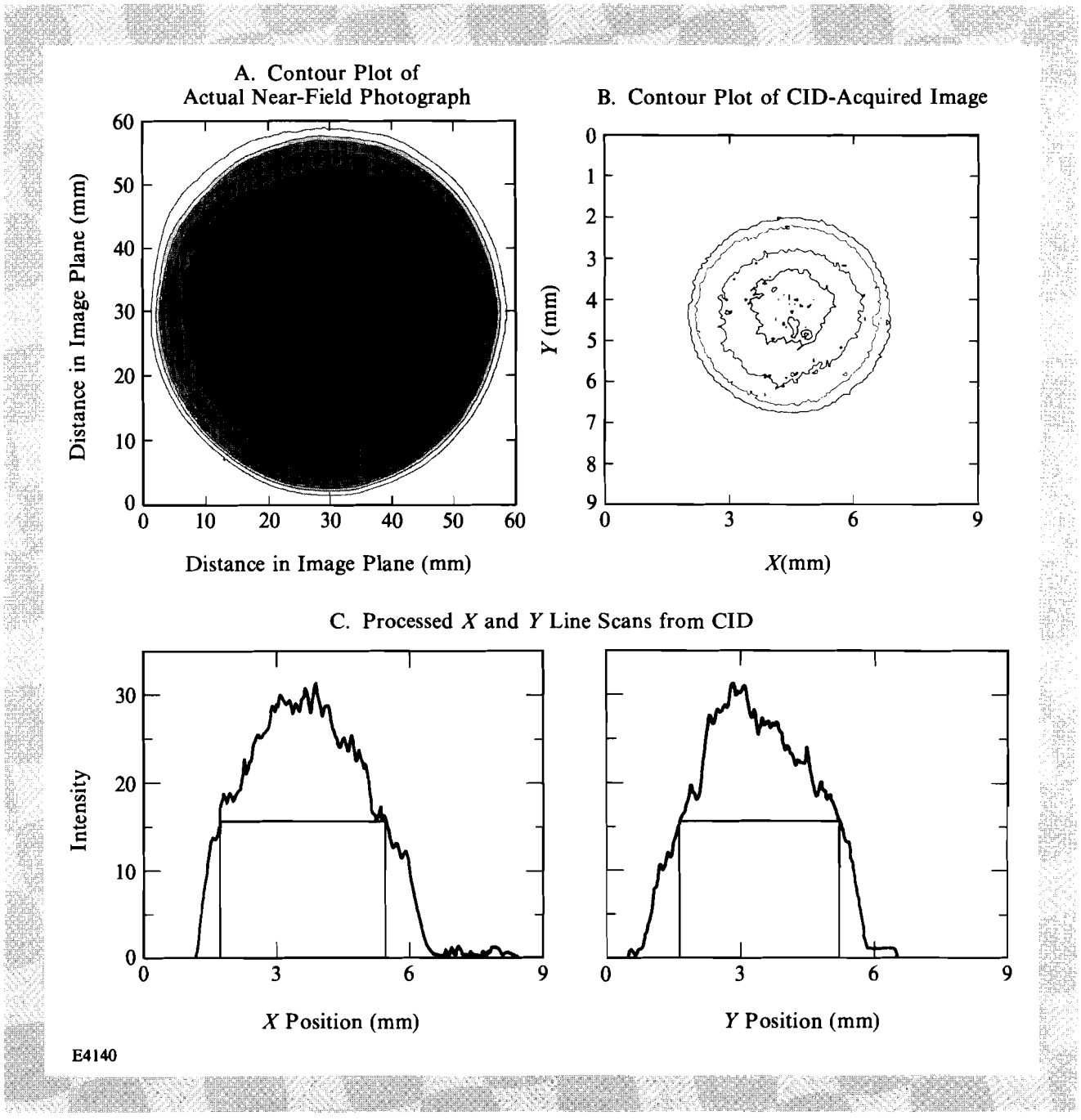

Fig. 29.24
CID beam profile diagnostic.

The multi-wavelength energy-sensing system (MESS) has been improved with new, high-reflectivity covers and calibrated with an accuracy approaching 2%. Such accuracy is required to obtain the beam balance and uniformity specification of the high-density target experiments.

Linear-polarizer/wave-plate combinations at the inputs to the beamline amplifiers have been replaced with liquid-crystal circular-polarizer/wave-plate combinations, providing high-contrast circular-polarized light into each amplifier stage. Tests of the device at the input of the 90-mm amplifiers show no damage to the liquid-crystal polarizers, and optimum polarization, even at high energies, for third-harmonic conversion.

As part of the effort to improve laser illumination uniformity, initial measurements were taken on beamline 6-2, the "perfect beam," which has been fitted with the finest optical components available and is completely covered by a turbulence-prevention corridor. A possible source of microthermals has been eliminated by removing the heat lamps that have been used to control the temperature of the frequency conversion crystals; instead, control is achieved by sensing the cell temperature and adjusting the phase-matching angle of the cell for optimum second- and third-harmonic conversion.

The ALPHA beam, previously called the 25th beam, has been successfully fired onto a target in the OMEGA target chamber. The ALPHA beam is transported through the laboratory from the output of

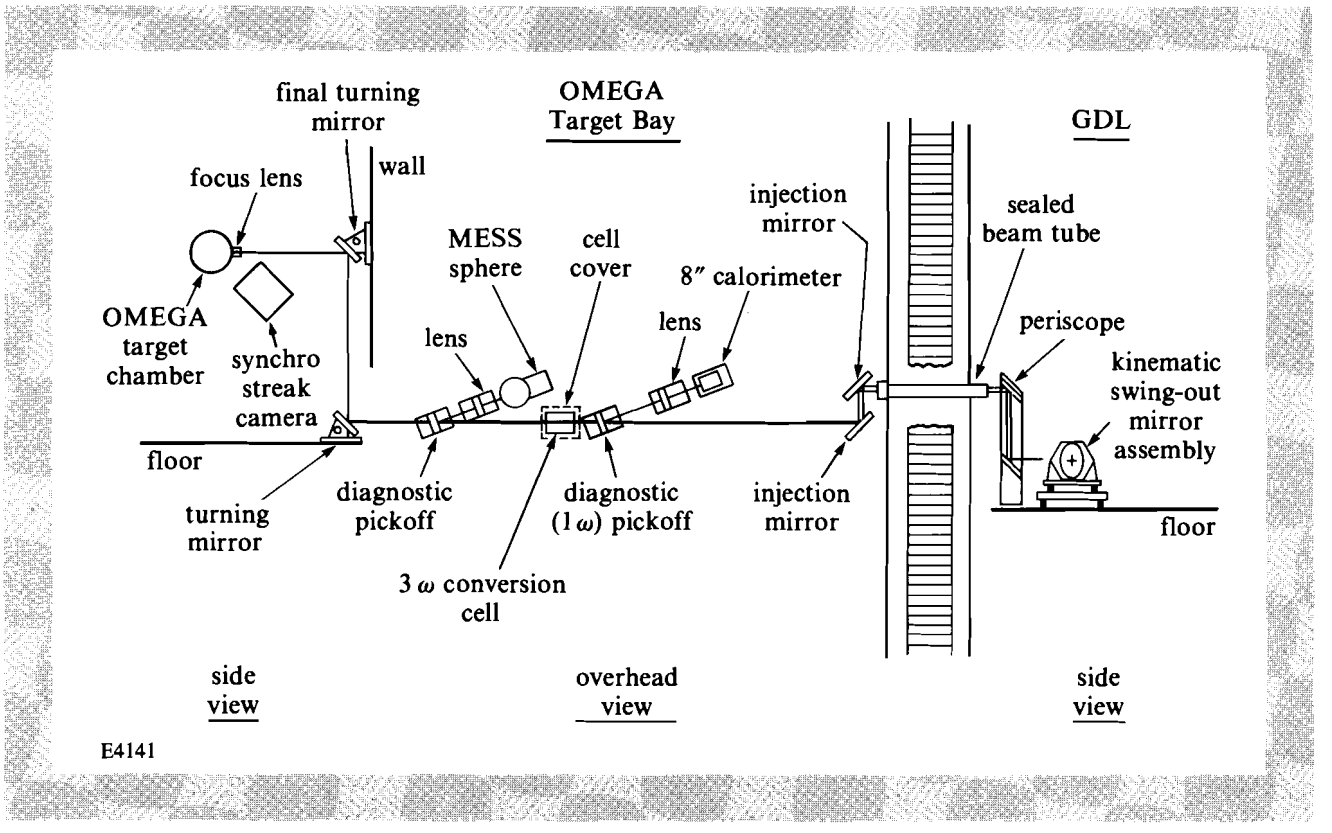

Fig 29.25
ALPHA beam layout.

the GDL/active mirror laser to the OMEGA target bay, as shown in Fig. 29.25. It will be used as a short-pulse, third-harmonic, x-ray backlighting source, synchronized with the OMEGA laser.

Target shots were taken for diagnostic activation and timing and in support of the National Laser Users Facility program.

A summary of OMEGA operations this quarter follows:

Driver Test and Alignment Shots	118
Beamline Tests	162
Target Shots	54
TOTAL	334

ACKNOWLEDGMENT

This work was supported by the U.S. Department of Energy Office of Inertial Fusion under agreement No. DE-FC08-85DP40200 and by the Laser Fusion Feasibility Project at the Laboratory for Laser Energetics, which has the following sponsors: Empire State Electric Energy Research Corporation, General Electric Company, New York State Energy Research and Development Authority, Ontario Hydro, and the University of Rochester. Such support does not imply endorsement of the content by any of the above parties.

PUBLICATIONS AND CONFERENCE PRESENTATIONS

Publications

S. D. Jacobs, A. L. Hrycin, K. A. Cerqua, C. M. Kennemore III, and U. J. Gibson, "Adhesion Enhancements and Internal Stress in MgF_2 Films Deposited with Ion Beam Assistance," *Thin Solid Films* **144**, 69–76 (1986).

G. Pien, M. C. Richardson, P. D. Goldstone, R. H. Day, F. Ameduri, and G. Eden, "Computerized 3-GHz Multichannel Soft X-Ray Diode Spectrometer for High-Density Plasma Diagnosis," *Nucl. Instrum. Methods B* **18**, 101–110 (1986).

K. L. Marshall, "Laser-Damage-Resistant Polysiloxane Polymers as Homeotropic Alignment Layers for Liquid Crystal Devices," *Mol. Cryst. Liq. Cryst. Lett.* **3**, 133–138 (1986).

M. C. Richardson, B. Yaakobi, R. Epstein, J. S. Wark, and J. M. Soures, "Imploding Cylindrical Plasmas as X-Ray Laser Media," *High Intensity Laser Processes* (SPIE, Bellingham, WA, 1986), Vol. 664, pp. 270–276.

R. S. Marjoribanks, P. A. Jaanimagi, and M. C. Richardson, "Principles of Streak and Framing Photography by Frequency-Encoding on a Chirped Pulse," *High Speed Photography, Videography, and Photonics IV* (SPIE, Bellingham, WA, 1986), Vol. 693, pp. 134–146.

U. Feldman, J. F. Seely, C. M. Brown, J. O. Ekberg, M. C. Richardson, W. E. Behring, and J. Reader, "Spectra and Energy Levels of Br XXV, Br XXIX, Br XXX, and BR XXXI," *J. Opt. Soc. Am. B* **3**, 1605–1608 (1986).

W. E. Behring, C. M. Brown, U. Feldman, J. F. Seely, J. Reader, and M. C. Richardson, "Transitions of the Type $2s$-$2p$ in Oxygenlike Y, Zr, and Nb," *J. Opt. Soc. Am. B* **3**, 1113–1115 (1986).

P. A. Holstein, J. Delettrez, S. Skupsky, and J. P. Matte, "Modeling Nonlocal Heat Flow in Laser-Produced Plasmas," *J. Appl. Phys.* **60**, 2296–2300 (1986).

J. F. Seely, J. O. Ekberg, C. M. Brown, U. Feldman, W. E. Behring, J. Reader, and M. C. Richardson, "Laser-Produced Spectra and QED Effects for Fe-like, Cu-like, and Zn-like Ions of Au, Pb, Bi, Th, and U," *Phys. Rev. Lett.* **57**, 2924–2926 (1986).

Forthcoming Publications

The following papers are to be published in the *Proceedings of the 17th Annual Boulder Damage Symposium*, Boulder, CO, October 1985:

K. A. Cerqua, S. D. Jacobs, B. L. McIntyre, and W. Zhong, "Ion Exchange Strengthening of Nd-Doped Phosphate Laser Glass."

B. Liao, D. J. Smith, and B. L. McIntyre, "The Development of Nodular Defects in Optical Coatings."

D. J. Smith, B. Krakauer, C. J. Hayden, A. W. Schmid, and M. J. Guardalben, "Yttrium-Oxide-Based Anti-Reflection Coating for High Power Lasers at 351 nm."

The following articles are to be published in *Laser Interaction and Related Plasma Phenomena Vol. 7,* edited by G. Miley and H. Hora (Plenum Press, New York, in press):

M. C. Richardson, P. W. McKenty, F. J. Marshall, C. P. Verdon, J. M. Soures, R. L. McCrory, O. Barnouin, R. S. Craxton, J. Delettrez, R. L. Hutchison, P. A. Jaanimagi, R. Keck, T. Kessler, H. Kim, S. A. Letzring, D. M. Roback, W. Seka, S. Skupsky, B. Yaakobi, and S. M. Lane, "Ablatively Driven Targets Imploded with the 24-UV-Beam OMEGA System."

M. C. Richardson, G. G. Gregory, R. L. Keck, S. A. Letzring, R. S. Marjoribanks, F. J. Marshall, G. Pien, J. S. Wark, B. Yaakobi, J. D. Goldstone, A. Hauer, G. S. Stradling, F. Ameduri, B. L. Henke, and P. A. Jaanimagi, "Time-Resolved X-Ray Diagnostics for High Density Plasma Physics Studies."

B. Yaakobi, O. Barnouin, C. B. Collins, R. Epstein, A. Hauer, S. A. Letzring, F. J. Marshall, R. L. McCrory, M. C. Richardson, J. M. Soures, and S. Wagel, "Laser-Generated X-Ray Studies Relevant to Compression Diagnostics and Nuclear Level Excitation."

W. C. Mead, S. V. Coggeshall, S. R. Goldman, E. K. Stover, P. D. Goldstone, A. Hauer, V. M. Kindel, L. Montierth, M. C. Richardson, O. Barnouin, P. A. Jaanimagi, R. S. Marjoribanks, R. L. Kauffman, H. Kornblum, and B. F. Lasinski, "Analysis, Modeling, and Design of Short Wavelength Laser Plasma Experiments."

B. Yaakobi, "X-Ray Diagnostic Methods for Laser-Imploded Targets" and "Thermal Transport, Mass Ablation, and Preheat in Laser-Target Experiments," to be published in the *Proceedings of the Spring College on Radiation in Plasmas,* Trieste, Italy, June 1985 (World Scientific Publishing Co.).

M. Guardalben, A. Schmid, M. Loudiana, and J. T. Dickinson, "Photothermal Analysis of Synergistic Radiation Effects in ThF_4 Optical Thin Films," to be published in the *Journal of Applied Physics.*

P. Bado, M. Bouvier, and J. S. Coe, "Nd:YLF Mode-Locked Oscillator and Regenerative Amplifier," to be published in *Optics Letters.*

J. C. Lee and S. D. Jacobs, "Refractive Index and $\Delta n/\Delta T$ of Cr:Nd:GSGG at 1064 nm," to be published in *Applied Optics.*

R. R. Whitlock, S. P. Obenschain, J. Grun, J. A. Stamper, J. A. Sprague, B. V. Sweeney, B. H. Ripin, and R. S. Craxton, "Flash *X* Radiography of Laser-Accelerated Foils," to be published in the *Journal of Applied Physics.*

J. F. Whitaker, T. Norris, G. A. Mourou, and T. Y. Hsiang, "Pulse Dispersion and Shaping in Microstrip Lines," to be published in *IEEE Microwave Theory and Techniques Society Transactions.*

S. H. Batha and C. J. McKinstrie, "Energy Cascading in the Beat-Wave Accelerator," to be published in a special issue of *IEEE Transactions on Plasma Science on Plasma-Based High-Energy Accelerators.*

D. R. Dykaar, R. Sobolewski, T. Y. Hsiang, and G A. Mourou, "Response of a Josephson Junction to a Stepped Voltage Pulse," to be published in *IEEE Transactions on Magnetics.*

J. M. Soures, R. L. McCrory, K. A. Cerqua, R. S. Craxton, R. Hutchison, S. D. Jacobs, T. J. Kessler, J. Kelly, G. Mourou, W. Seka, and D. Strickland, "High Power Laser Research and Development at the Laboratory for Laser Energetics," to be published in the *Proceedings of the SPIE's Fiber LASE Applications in Science and Engineering '86 Symposium,* Cambridge, MA, September 1986.

H. L. Helfer and R. L. McCrory, "Some Properties of a Polarized OCP," to be published in *Strongly Coupled Plasmas*, edited by Forest Rogers and Hugh DeWitt (Plenum Press, New York).

G. Mourou, "Picosecond Electro-Optic Sampling," to be published in the *Proceedings of the High Speed Electronics Conference*, Stockholm, Sweden, August 1986.

Conference Presentations

G. A. Mourou, "Femtosecond Optics for the Characterization of Terahertz Electronics," presented at the Electron Device Activities in Western New York Conference, Rochester, NY, October 1986.

The following presentations were made at the 1986 Optical Society of America Annual Meeting, Seattle, WA, October 1986:

S. D. Jacobs, D. G. Angeley, D. S. Smith, and J. C. Lampropoulos, "Thermal Conductivity Measurements of Dielectric Thin Films on Optical Substrates."

D. Strickland, P. Maine, and G. Mourou, "Generation of Ultrahigh Peak Power Pulses with the Technique of Chirped Pulse Amplification."

The following presentations were made at the 33rd National Symposium of the American Vacuum Society, Baltimore, MD, October 1986:

H. Kim and M. Wittman, "X-Ray Microscopy of Inertial Fusion Targets Using a Laser-Produced Plasma as an X-Ray Source."

S. Gracewski and R. Gram, "Analysis of Forces on ICF Targets During Ablation Layer Coating."

The following presentations were made at the Annual Fall Meetings, Glass, Basic Science, and Electronics Division, The American Ceramic Society, New Orleans, LA, November 1986:

K. A. Cerqua, S. D. Jacobs, and A. Lindquist, "Subsurface Damage Treatments for Ion-Exchange-Strengthened Phosphate Laser Glass."

S. D. Jacobs, R. S. Craxton, R. J. Hutchison, D. J. Smith, W. S. Beich, W. Seka, K. J. Skerrit, T. J. Kessler, K. A. Cerqua, and K. L. Marshall, "Materials Issues for Efficient Frequency Tripling in High-Peak-Power Nd:Glass Lasers" (invited).

R. L. McCrory, J. M. Soures, P. Audebert, O. Barnouin, R. S. Craxton, J. Delettrez, R. Epstein, L. Forsley, R. Hutchison, R. Keck, T. Kessler, S. Jacobs, H. Kim, S. A. Letzring, R. Marjoribanks, F. Marshall, P. W. McKenty, G. A. Mourou, M. C. Richardson, W. Seka, R. W. Short, A. Simon, S. Skupsky, K. Swartz, C. Verdon, J. Wark, B. Yaakobi, and P. A. Jaanimagi, "Direct-Drive Laser Fusion in the U.S.," presented at the 11th International Conference on Plasma Physics and Controlled Nuclear Fusion Research, Kyoto, Japan, November 1986.

The following presentations were made at the APS Conference, Baltimore, MD, November 1986:

P. Audebert, O. Barnouin, J. Delettrez, R. Epstein, R. S. Marjoribanks, F. J. Marshall, M. C. Richardson, and B. Yaakobi, "Space-Resolved X-Ray Spectra of Imploding Laser Fusion Targets."

O. Barnouin, B. Yaakobi, and L. M. Goldman, "Origin of the Different Burn-Throughs Observed for Silicon and Calcium in Thermal Transport Experiments."

S. Batha, W. Seka, L. M. Goldman, A. Simon, R. W. Short, R. Bahr, and W. Lockman, "Enhanced Thomson Scattering from Laser Plasmas."

D. K. Bradley, A. Rankin, J. S. Wark, J. Lunney, J. Armstrong, R. W. Eason, A. Hauer, J. D. Kilkenny, A. Cullis, and U. Zammit, "Time-Resolved X-Ray Diffraction from Silicon During Pulsed Laser Annealing."

R. S. Craxton and R. L. McCrory, "Hydrodynamic Simulations of Nonuniformly Irradiated Targets."

J. Delettrez, R. Epstein, P. A. Jaanimagi, M. C. Richardson, and S. Skupsky, "Simulation of Recent Transport Experiments at LLE."

R. Epstein, J. Delettrez, S. Skupsky, and B. Yaakobi, "Non-LTE Radiation and Ion-Dynamic Effects in Hydrodynamic Simulations of Laser-Driven Plasmas."

G. G. Gregory, L. B. DaSilva, P. A. Jaanimagi, S. A. Letzring, P. W. McKenty, and M. C. Richardson, "Time-Resolved Photography of Spherical Targets Irradiated with 24 UV Beams."

P. A. Jaanimagi, J. Delettrez, O. Barnouin, L. DaSilva, R. Epstein. F. J. Marshall, M. C. Richardson, and B. Yaakobi, "Re-Interpretation of Thermal Transport Experiments on OMEGA."

R. S. Marjoribanks, P. Audebert, L. DaSilva, J. Delettrez, R. Epstein, G. Gregory, P. A. Jaanimagi, and M. C. Richardson, "Time-Resolved Temperature and Density Measurements in Ionizing, Uniformly Irradiated UV-Laser-Produced Plasmas."

F. J. Marshall, P. A. Jaanimagi, S. A. Letzring, R. L. McCrory, P. W. McKenty, M. C. Richardson, J. M. Soures, C. P. Verdon, and J. S. Wark, "Interpretation of Experimental Results of High-Aspect-Ratio Laser Fusion Target Implosions."

M. C. Richardson, P. Audebert, G. G. Gregory, P. A. Jaanimagi, R. J. Hutchison, R. Kremens, H. Kim, S. A. Letzring, F. J. Marshall, R. L. McCrory, P. W. McKenty, J. M. Soures, and C. P. Verdon, "Dynamics of Ablatively Driven Solid-Shell Targets on OMEGA."

W. Seka, R. Bahr, L. M. Goldman, F. J. Marshall, K. Swartz, R. W. Short, and A. Simon, "Investigation of the Spectral and Spatial Emission Characteristics Between Half and Twice the Laser Frequency of Uniformly Illuminated Spherical Laser Plasmas."

A. Simon, "Interpretation of Raman Spectral Observations."

C. P. Verdon, P. A. Jaanimagi, S. A. Letzring, F. J. Marshall, R. L. McCrory, P. W. McKenty, M. C. Richardson, J. M. Soures and J. S. Wark, "Theoretical Interpretation of OMEGA High-Yield and High-Density Implosion Experiments."

J. S. Wark, J. Delettrez, P. W. McKenty, M. C. Richardson, J. M. Soures, and C. P. Verdon, "Alpha Particle Imaging of High-Yield Implosions."

N. Delamater, A. Hauer, C. F. Hooper, T. Garber, M. Richardson, P. Jaanimagi, O. Barnouin, and R. L. Kauffman, "Spectroscopic Analysis of 0.35-Micron OMEGA Implosions of Kr/Ar-Filled Plastic Shells."

P. D. Goldstone, S. R. Goldman, W. C. Mead, J. A. Cobble, M. C. Richardson, F. J. Marshall, R. S. Marjoribanks, and P. A. Jaanimagi, "Dynamics of Short-Wavelength Laser-Produced High-Z Plasmas: An Update."

A. Hauer, N. Delamater, P. Audebert, O. Barnouin, G. Gregory, P. Jaanimagi, F. J. Marshall, M. C. Richardson, B. Yaakobi, and

D. Dustin, "Development of X-Ray Diagnostics for Ultraviolet Laser Implosions."

J. C. Moreno, H. R. Greim, S. Goldsmith, A. Krumbein, R. Epstein, M. Richardson, and B. Yaakobi, "Thermal Transport Studies of 351-nm Laser-Produced Plasmas Using EUV Spectroscopy."

S. Skupsky, "Coulomb Logarithms."

R. W. Short, "Stimulated Raman Scattering in Self-Focused Light Filaments in Laser-Produced Plasmas."

B. Yaakobi, "Recent Progress in X-Ray Laser Studies at the Laboratory for Laser Energetics," presented at the ISTO Ultra Short Wavelength Laser Technical Review, Washington, DC, December 1986.

H. E. Elsayed-Ali and G. A. Mourou, "Time-Resolved Phase Transitions in the Picosecond Time Domain," presented at the 1986 Fall Meeting of the Materials Research Society, Boston, MA, December 1986.

ACKNOWLEDGMENT

The work described in this volume includes current research at the Laboratory for Laser Energetics, which is supported by Empire State Electric Energy Research Corporation, General Electric Company, New York State Energy Research and Development Authority, Ontario Hydro, the University of Rochester, and the U.S. Department of Energy Office of Inertial Fusion under agreement No. DE-FC08-85DP40200.